UNLV Theses, Dissertations, Professional Papers, and Capstones

Cretaceous and Eocene U-Pb Zircon Migmatite Ages from the East Humboldt Range Metamorphic Core Complex, Nevada

Jordan Drew

University of Nevada, Las Vegas, jordanw.drew@gmail.com

Repository Citation

CRETACEOUS AND EOCENE U-PB ZIRCON MIGMATITE AGES FROM THE EAST HUMBOLDT

RANGE METAMORPHIC CORE COMPLEX, NEVADA

By

Jordan Drew

Bachelor of Arts
University of Kentucky
2009

A thesis submitted in partial fulfillment
of the requirements for the

Master of Science in Geoscience

Department of Geoscience
College of Sciences
The Graduate College

University of Nevada, Las Vegas
May 2013

THE GRADUATE COLLEGE

We recommend the thesis prepared under our supervision by

Jordan Drew

entitled

Cretaceous and Eocene U-Pb Zircon Migmatite Ages from the East Humboldt Range
Metamorphic Core Complex, Nevada

be accepted in partial fulfillment of the requirements for the degree of

Master of Science in Geoscience

Department of Geoscience

Rodney Metcalf, Ph.D., Committee Chair

Michael Wells, Ph.D., Committee Member

Terry Spell, Ph.D., Committee Member

George Rhee, Ph.D., Graduate College Representative

Tom Piechota, Ph.D., Interim Vice President for Research &

Dean of the Graduate College

May 2013

ABSTRACT

Zircon separates from migmatite samples from the East Humboldt Range (EHR), northern Nevada were U-Pb dated using secondary ionization mass spectrometry. Cathodoluminescence images of zircons show bright anhedral cores with abundant euhedral overgrowths surrounding them.

The overgrowths give U-Pb dates indicating two periods of zircon growth. Inner rims have a Cretaceous age population at 70.6 ± 2.6 Ma. Outer rims give Eocene ages that either fall in to a single-age population at 45 ± 1.3 Ma or are part of a range from 41-31 Ma. Discordant zircon cores have upper intercepts between 1.8 -1.0 Ga.

Cretaceous and Eocene ages are interpreted as recording protracted growth of anatectic zircon during Mesozoic thrust burial and Cenozoic regional extension. McGrew et al. (2000) reported a U-Pb TIMS age of 84.8 ± 2.8 Ma on zircons from the EHR, while Premo et al. (2008) reported ion probe ages of 90-71 Ma from zircons in the same area.

TABLE OF CONTENTS

LIST OF TABLES

LIST OF FIGURES

CHAPTER 1: INTRODUCTION

Migmatites are partially melted rocks that record periods of high-grade metamorphism, generally in the middle crust. Partial melting is increasingly being recognized as an important part of orogenesis because migmatites are major structural components of orogenic belts. Orogenic belts are cored by migmatites, and eventually, slowly collapse due to the weak rheology of partially molten crust. During crustal extension, migmatitic metamorphic core complexes can be unroofed and brought to the Earth's surface in the footwalls of large-offset normal faults.

Core complexes provide important information about the mid- to lower-crustal conditions of the orogenic belt during and after orogenesis (Kruckenberg et al., 2008). Pressure and temperature can be interpreted from metamorphic assemblages, pervasiveness of partial melting can often be seen, and metamorphic fabrics can be studied.

The East Humboldt Range (EHR) in northern Nevada (Fig. 1) contains an exposed metamorphic core complex, which is the result of two independent tectonic events, (1) Sevier-aged thrusting, which produced migmatites and (2) regional extension, which exposed the core complex in the footwall of a large-offset normal fault (Hodges et al., 1992; Wright and Snoke, 1993; McGrew et al., 2000; DeCelles, 2004; Howard et al., 2011). In this study, migmatites exposed at Angel Lake in the northern EHR were analyzed in order to understand the timing of metamorphism in the mid-crustal zone of the EHR metamorphic core complex. Understanding the timing of metamorphism within the EHR offers insight into the regional tectonic history and the significance of regional tectonic thrusting and extension relative to the production of core complex migmatites.

The primary goal of this thesis is to understand the timing of partial melting and metamorphism within the EHR core complex. In order to date the crystallization of in-situ melts,

zircon separates from migmatites were dated using U-Pb analysis. Stromatic (or layered) migmatites were sampled because they are thought to record partial melts retained in source rocks under high-strain conditions, thereby dating anatexis (Vernon and Clarke, 2008). Determining the source of mobile melts can be difficult, so in-situ melts are the best candidates for dating locally-sourced migmatization and metamorphism.

Migmatites are comprised of the leucosome (formed by crystallization of accumulated melt), melanosome (residual solids from partial melting, sometimes referred to as "restite") and paleosome (original rock with little to no melting) (Sawyer, 2008). By comparing the ages of the inherited zircon cores of the leucosome and melanosome to those of the paleosome, it can be determined whether the leucosome and melanosome were formed from the paleosome, or whether they were injected melts. If the zircon core ages match, then it can be inferred that the melts were localized and didn't migrate far from their source.

A secondary goal of this study is to look at melt segregation of the migmatites. In traditional melt segregation models, it is thought that melt moves down pressure gradients associated with deformation, with melanosomes representing sites of melt extraction and leucosomes as sites of melt accumulation. This deformation-assisted melt segregation (DAMS) model predicts that the melanosome should contain inherited zircon that didn't precipitate from the partial melting event, while the leucosome should have new-growth zircon that crystallized from the melt (Sawyer, 1996). This study looks at zircons from a full suite of stromatic migmatites (leucosome, melanosome and paleosome) to determine whether the melts follow a purely mechanical separation technique (as described above) or whether there is evidence for an alternative segregation model.

CHAPTER 2: GEOLOGIC BACKGROUND

The East Humboldt Range and the Ruby Mountains are located in northeastern Nevada and together form a metamorphic core complex with a protracted Mesozoic to Cenozoic metamorphic and tectonic history. This core complex is located in the northern Basin and Range province and lies in the hinterland of the Sevier fold-and-thrust belt (Fig. 1). Many studies have focused on the nature and age of tectonic events in the Ruby Mountains-East Humboldt Range metamorphic core complex (Lush, 1988; Hodges et al., 1992; McGrew, 1992; Wright and Snoke, 1993; Peters and Wickham, 1994; McGrew et al., 2000; Premo et al., 2008). While general timing of regional burial and extension has been established, more data are needed to constrain accurate timing and duration of migmatization, which can be used to infer timing of high-grade metamorphism and related tectonic events. This study focuses on migmatites in the EHR and uses ion probe U-Pb dating of zircons coupled with cathodoluminescence (CL) imaging to gather this information.

The East Humboldt Range is a tectonically complex area. A major structure in the EHR is a recumbent fold, named the Winchell Lake nappe. In the core of the fold are Neoarchean orthogneiss and Paleoproterozoic paragneiss (Lush et al., 1988; Henry et al., 2011). Around the gneissic core is a package of quartzite, marble and pelitic schist whose protoliths are inferred to be Neoproterozoic to Mississippian sedimentary rocks (McGrew et al., 2000). Migmatites, as well as late-stage plutons, can be seen throughout the metasedimentary rock units. Due to shearing by a low-angle normal fault, extensive mylonitization is now visible in the footwall of the metamorphic core complex, especially in the western half of the range (Fig. 1) (Wright and Snoke, 1993). In the northern EHR, at Angel Lake, the core and both upper and lower limbs of

the Winchell Lake nappe are exposed. The fold closes approximately seven kilometers south at Lizzies Basin (Fig. 1).

A simplified geologic map shows some of the rock types present (Fig. 1) (modified from Miller and Snoke, 2009). This map has incorporated all Proterozoic rocks (gneisses, schists and calc-silicates) and Neoproterozoic to Mississippian metasedimentary rocks into one unit labeled "Ruby Mountains-East Humboldt Range igneous and metamorphic complex", which houses the pervasive migmatites. Figure 2 provides a more detailed look at the Angel Lake cirque area (denoted by a red star in Fig. 1).

Neoarchean orthogneiss and Paleoproterozoic paragneiss (McGrew et al., 2000) form the core of the Winchell Lake nappe. Zircon fractions from the orthogneiss yielded U-Pb dates with an upper intercept of 2520 ± 110 Ma, and a lower intercept at 196 ± 32 Ma (Lush et al., 1988). The upper intercepts give an Archean crystallization age for the orthogneiss protolith, but due to the complicated tectonic history of the complex, and the possibility of multiple stages of Pb loss, the lower intercept of 196 Ma likely does not have any real age significance (Lush et al., 1988). Premo et al. (2008) used a sensitive high-resolution ion microprobe (SHRIMP) to date zircons from the orthogneiss, which gave a best-fit mean $^{207}Pb/^{206}Pb$ age of 2531 ± 19 Ma from zircon cores. McGrew and Premo (2011) report SHRIMP dates from orthogneiss zircon of 2449 ± 3.0 Ma from zircon cores.

Folded around and enveloping the core of orthogneiss and paragneiss is a section of quartzite, pelitic schist and marble interpreted to be metamorphic equivalents of Neoproterozoic to Mississippian miogeoclinal sedimentary rocks of the eastern Great Basin (McGrew, 1992; Lush et al., 1988). The sedimentary rocks were continuously metamorphosed during Mesozoic burial and Cenozoic regional extension and now form the upper and lower

limbs of the Winchell Lake nappe (Lush et al., 1988; Hodges et al., 1992; Wright and Snoke,

1993; McGrew et al., 2000; Henry et al., 2011)).

During the Sevier orogeny (middle to late Mesozoic), the region underwent thrust burial

and reached amphibolite-grade metamorphic conditions beginning prior to the Late Cretaceous

(Camilleri and Chamberlain, 1997; McGrew et al., 2000; DeCelles, 2004) and perhaps as early as

Late Jurassic (Hodges et al., 1992). It has been hypothesized that during convergence, the

thickened middle crust was thermally weakened and had begun plastically deforming and

flowing by the Late Jurassic (Hodges et al., 1992). Thickening of the crust likely led to a heating

event, with magmas (dated at approximately 153 Ma), sourced at depth and injected at current

exposure levels (Hudec, 1990; Lee et al., 2003; DeCelles, 2004; Premo et al., 2008).

McGrew et al. (2000) summarized available thermobarometric and geochronologic data

for the East Humboldt Range, as discussed below. They stated that peak metamorphism was

achieved in the Late Cretaceous, which overprinted the earlier Jurassic metamorphic fabrics. P-T

conditions during peak metamorphism were >9 kbar and approximately 800°C. At these

conditions, the temperature was high enough to initiate dehydration partial melting of biotite.

Premo et al. (2008) reported SHRIMP dates from orthogneiss zircon overgrowths (whose cores

were Neoarchean-aged) of 91-72 Ma. Premo et al. (2008) interpreted the 90 Ma age to be the

time of crystallization, and the spread of ages to be the result of Pb loss. Thermal ionization

mass spectrometry (TIMS) analyses of zircon separates from leucogranite in a metapelitic schist

layer from the hinge zone of the Winchell Lake nappe yielded a ^{207}Pb/^{206}Pb age of 84 ± 2.8 Ma,

which is thought to date the metamorphic event (McGrew et al., 2000). The abundance of the

leucogranite in the schist, but not in adjacent marbles, suggests that the melt originated in-situ;

and the abundance of leucogranite in the hinge zone of the fold suggests that the melt was

synkinematic with nappe emplacement (McGrew et al., 2000). Therefore, migmatization

accompanied nappe emplacement in the Late Cretaceous. The folding event placed

Neoproterozoic to Paleozoic metasedimentary rocks in the upper and lower limbs of the nappe.

Exhumation occurred dominantly in the late Eocene following the final stages of the

Sevier orogeny, with high-angle detachment faults forming and upper-amphibolite facies

conditions in the middle crust (Miller and Snoke, 2009). The P-T-t path followed a clockwise

loop, with rapid decompression from peak P-T conditions of >9 kbar and 800°C to 5 kbar and

630°C during Eocene extension (Kistler et al., 1981; Thorman and Snee, 1988; Hudec, 1990;

Hurlow et al., 1991; Hodges et al., 1992; McGrew, 1992; Peters and Wickham, 1994; Camilleri

and Chamberlain, 1997; McGrew et al., 2000) (Figure 5B from McGrew et al., 2000). Wells and

Hoisch (2008) suggested regional Late Cretaceous exhumation related to mantle delamination

prior to 50-63 Ma, perhaps leading to >2.5 kbar of the decompression. This rapid

decompressional trend indicates nearly isothermal unroofing consistent with rapid exhumation.

During this unroofing event, a top-to-the-west-northwest mylonitic shear zone fabric permeated

much of the core complex (Wright and Snoke, 1993) (Fig. 1). The mylonitic rocks had cooled

through the biotite closure temperature by 24-22 Ma (Dallmeyer et al., 1986), and they had

cooled through the zircon closure temperature for annealing fission tracks by 25-23 Ma (Dokka

et al., 1986). According to McGrew and Snee (1994), discordant $^{40}Ar/^{39}Ar$ age spectra from

hornblende from high structural levels in the EHR give ages from 63-49 Ma and 36-29 Ma from

lower structural levels, while $^{40}Ar/^{39}Ar$ data from biotite, muscovite and potassium feldspar yield

cooling ages of 27-21 Ma for all structural levels.

Peters and Wickham (1994) studied the amphibolite-facies marbles of the

Neoproterozoic to Mississippian metasedimentary sequence in the EHR. Three separate marble

assemblages were found which equilibrated at approximately 6 kbar and 650-700°C in a high

X_{CO2} mixed-volatile fluid. The marbles equilibrated post-peak metamorphism, and the H_2O fluid

supplied to the system is assumed to have originated in pegmatitic leucogranites, found

abundantly on the west flank of the core complex.

U-Pb dates from zircon and monazite indicate that a protracted interval of plutonism

occurred between 40 and 29 Ma, with compositions ranging from quartz diorite to leucogranite

(Wright and Snoke, 1993). Howard et al. (2011) reported SHRIMP dates of 38-29 Ma from the

orthogneiss zircon overgrowths, which correlate with this Wright and Snoke (1993) data. Many

of these plutons were deformed and mylonitized during regional extension. Monazite grains

from plutonic bodies within the mylonitic shear zone have been dated using U-Pb isotopes at 39

Ma to 29 Ma (Wright and Snoke, 1993). Due to regional extension and erosion, migmatites of

the recumbent fold are now visible at the surface from Angel Lake to Lizzies Basin along the east

flank of the East Humboldt Range.

CHAPTER 3: ZIRCON BEHAVIOR DURING ANATEXIS

Many studies have been conducted relating to the solubility of zircon in silicate melt during high-grade metamorphism and partial melting (Watson et al., 1989; Watt and Harley, 1993; Watt et al., 1996; Vavra et al., 1996, Bea and Montero, 1999; Vavra et al., 1999). Watson and Harrison (1983) and Harrison and Watson (1983) showed experimentally that for crustally-derived silicic melts, the main controls on zircon solubility are temperature and melt composition. For a given temperature and composition, Zr concentration in the melt can be solved for in this experimentally-derived equation:

$$C_{Zr}(melt) = C_{Zr}(zircon) * \exp[3.80 + 0.85(M-1) - 12900/T]$$

For this equation, the concentration of Zr in zircon is approximately 476,000 ppm (Miller et al., 2003). M represents the cation ratio (Na+K+2Ca)/Al*Si, and T is absolute temperature.

In a peraluminous melt, where M=1.3, Zr solubility is 24 ppm at 650°C, 96 ppm at 750°C and 295 ppm at 850°C (Watson, 1996). For a metaluminous melt with M=1.7, Zr solubility is 33 ppm at 650°C, 129 ppm at 750°C and 396 ppm at 850°C. This equation shows that Zr solubility in silicate melts increases with temperature, but decreases when the melt is more aluminous.

During an anatectic, high-grade metamorphic event, partial melts may develop. If zircon is present in the system prior to the onset of anatexis, it will dissolve until the melt reaches saturation. Inherited zircon is preserved if the melt becomes saturated in Zr or if the grains are shielded from the melt as inclusions. This process occurs in a geologically short time interval – Watson (1996) showed experimentally that zircon will dissolve in a silicate melt in a matter of days. In the EHR, where temperatures reached 800° C during peak metamorphism (McGrew et al., 2000), it can be inferred that the inherited zircon was saturating the anatectic melt with approximately 300 ppm Zr.

Smaller zircon grains have a larger surface area per unit volume, therefore increasing those grains' Gibbs free energy. To minimize the interfacial free energy of the system, the smallest zircons preferentially dissolve into a melt first. Once the melt becomes oversaturated in Zr, or when temperature decreases, recrystallization occurs. The Zr preferentially goes into zircon, which crystallizes on larger surviving inherited grains of zircon. Most decoupled dissolution-precipitation of zircon occurs post-peak metamorphism, although relative timing of recrystallization is dependent on water content of the melt (Harley et al., 2007). Melts that are more water-saturated tend to crystallize at lower temperatures than dry melts.

Coupled dissolution-precipitation may occur if hydrous fluids interact with the zircon. As the Zr-saturated fluid becomes oversaturated, zircon systematically recrystallizes as more Zr is dissolving into the fluid. (This is in contrast to decoupled dissolution-precipitation where zircon doesn't recrystallize immediately at the site of dissolution.) These fluids can come from melting water-rich minerals (such as hornblende or biotite), or they may be part of an influx not originating in the system. Fluid interaction can occur at any point during metamorphism, although the effects aren't usually preserved unless the recrystallization is late-stage. Recrystallization can occur around the outer rim of a zircon grain, it can propagate as "fronts" through a grain, or it may pervade the crystal if there are fractures (e.g., Fig. 2 in Harley et al., 2007).

CHAPTER 4: METHODS

This study used zircon separates from migmatites to conduct secondary ionization mass spectrometer (SIMS) geochronology. In order to obtain zircon mineral separates, samples were collected at immediately west of Angel Lake in the northern EHR (Fig. 2). Migmatites were sampled from a migmatitic metasedimentary unit of quartzite and pelitic schist (unit CZqs in Fig. 2) thought to represent a Neoproterozoic to early Cambrian sedimentary stratigraphic sequence (McGrew et al., 2000; Henry et al., 2011). Stromatic migmatites (Fig. 3), which feature alternating horizontal layers of leucosome and melanosome, were chosen because of the likelihood that they represent in-situ partial melts, thereby dating anatexis rather than injection. Sampling stromatic migmatites is important because of the contiguous leucosome-melanosome pairs, thought to represent genetically related in-situ melts and residual solids, respectively. One such melt-restite pair was sampled at Angel Lake, sample 107-1 (Fig. 3A). Sometimes the paleosome, or unmelted portion, of the migmatite is also present. In the case of the EHR samples, the lithologies within the metasedimentary unit changes often, sometimes even over hand-sample scale. Sample 107-4 is a being called a contiguous melt-restite-paleosome triplet (Fig. 3B), however the quartzite paleosome is not the source of the main partial melts, but is the best example of an unmodified protolith. It is used as a proxy to demonstrate, through U-Pb dating of zircons, that melts are locally derived and not injected. The locations of sampled migmatites are shown in Figures 1 and 2, and in Table 1.

Samples 107-1 and 107-4 were sawed into 1-inch slabs, which were cut further to make billets for thin section of samples 107-1L (leucosome), 107-1M (melanosome), 107-4L (leucosome), 107-4M (melanosome) and 107-4Q (quartzite paleosome). Billets were sent off to be made into thin sections, which were then analyzed on a petrographic microscope with transmitted light to determine representative mineralogy.

Other slabs sawed from samples 107-1 and 107-4 were sawed again perpendicular to original cuts, separating the leucosome, melanosome and quartzite paleosome (although sample 107-1 did not have an associated paleosome). This produced five samples: 107-1L (leucosome), 107-1M (melanosome), 107-4L (leucosome), 107-4M (melanosome) and 107-4Q (paleosome). These samples were crushed into very small pebble-sized pieces in a rock crusher. The melanosomes had thin domains of quartzofeldspathic and/or muscovite layers and the leucosomes had some thin layers of melanosome material, so the contaminating lithologies were hand-picked out of the crushed samples. Biotite-rich melanosomes were further crushed by hand using an agate mortar and pestle to release zircon that had crystallized in biotite.

Crushed samples were washed to eliminate extremely fine powder and baked at 100°C overnight to dry. The samples were then sieved into two size fractions (<250μm and >250μm). A hand magnet was used to separate the bulk of magnetic minerals from the non-magnetic portion. The non-magnetic portion of both size fractions of the samples was then stirred in methylene iodide (a "heavy liquid" which separates minerals based on density) in a separatory flask under a fume hood. Minerals that settled to the bottom of the flask were sieved out first and labeled as "sinks," while the minerals that were less dense were sieved out last and labeled as "floats." Zircons were separated using standard gravimetric and magnetic separation techniques, and were then hand-picked and put into small vials.

The vials of zircon grains were sent to the SIMS laboratory at the University of California, Los Angeles for mounting and CL imaging using a scanning electron microscope (SEM). U-Pb dating was performed according to the procedure outlined in Schmitt et al. (2003). The zircons were mounted in epoxy, polished with 1 μm Al_2O_3 to expose the grains' interiors, ultrasonically cleaned and then coated in approximately 10 nm of gold. A Leo 1430VP SEM was used for CL imaging. U-Pb dates were obtained using the UCLA CAMECA Secondary Ionization Mass

Spectrometer (SIMS) 1270 ion probe. The mounted grains were probed with a 10–20 nA $^{16}O^-$

beam focused to a ~15–20 μm diameter spot. Spots for analysis were chosen from the CL

images, based on size of internal zonation and lack of internal defects such as cracks or

inclusions.

CHAPTER 5: RESULTS

5.1 Thin Sections

Leucosome sample 1L is dominated by sub-equal amounts of quartz, K-feldspar and plagioclase with accessory titanite, and secondary muscovite and chlorite (Fig. 4A). Multi-grain quartz ribbons, or shear bands, are composed of elongate undulose quartz grains exhibiting grain boundary migration features. Quartz ribbons are co-planar with wavy micaceous foliation domains. Feldspars are subhedral against quartz ribbons and exhibit both undulose extinction and brittle-deformation fractures. Muscovite is found along shear bands and fractures in feldspar. Small amounts of sillimanite are present in the foliation with the muscovite. No igneous crystallization textures are evident due to sub-solidus deformation features.

Melanosome sample 1M's mineralogy is dominantly biotite with quartz and plagioclase, along with traces of orthoclase, muscovite, garnet and sillimanite (Fig. 4B). The biotite is coarse-grained, with some grains being bent, defining the foliation. Biotite is strongly pleochroic from red to brown. Zircons can be found in some biotite grains surrounded by pleochroic halos. There are highly strained, undulose quartz ribbons elongate parallel to foliation. Plagioclase exhibits albite twinning. Sillimanite is found in association with the biotite, and is fibrolitic to prismatic. There are traces of very small muscovite grains intergrown with biotite. Garnet is subhedral to anhedral, fractured and contains quartz and biotite inclusions.

Leucosome sample 4L has very coarse K-feldspar and plagioclase grains, medium to fine grained quartz, muscovite and biotite filled veins (Fig. 4C). Feldspars show brittle fractures and plagioclase exhibits albite twinning. Quartz is present in a multiple elongate grains with undulose extinction and exhibit grain boundary migration features. There are small traces of sillimanite in the muscovite. Several plagioclase grains in this sample are subhedral with elongate lath-shape typical of igneous crystallization (Fig. 4C).

Melanosome sample 4M has interspersed strained mica-rich domains (muscovite +

biotite) and quartzofeldspathic domains (Fig. 4D). The plagioclase is strained with albite

twinning. Muscovite comprises approximately 20% of the mica present, in contrast to sample

1M, which has only trace amounts. Zircon grains are found within biotite.

The quartzite paleosome sample 4Q is predominantly undulose quartz, with minor

twinned plagioclase and mica present (Fig. 4E). Trace amounts of opaque oxides are also

present, appearing as darker bands in hand sample (Fig. 3B) Zircon can be found as inclusions in

both plagioclase and biotite.

5.2 Zircon Images and Morphologies

Cathodoluminescence images of zircon grains revealed complex internal structures,

such as growth zones and dissolution surfaces (Fig. 5A, Fig. 6A, Fig. 7A, Fig. 8A, Fig. 9A). Nearly

all grains display two distinct components, (1) a central core and (2) overgrowths (also referred

to as "rims") surrounding the core. Zircon cores are generally subhedral to anhedral to rounded,

and produce bright CL images showing little to no zoning. The exceptions are cores from sample

107-1M which produced darker CL images and exhibit convolute zoning. Many zircon

overgrowths have euhedral oscillatory zoning, which represents the external crystal shape

during successive growth stages; however, some overgrowths are show little zoning. External

morphologies of dated zircons are predominantly euhedral, with some grains exhibiting

subhedral shapes. Euhedral grains have elongated prisms and dipyramidal terminations. An

exception are zircon grains from sample 107-4Q, where external morphologies are subhedral to

anhedral (Fig. 9A). Some grains have dissolution surfaces visible within the rims, indicating

different generations of growth. The U-Pb dates were obtained from both the zircon cores and

zircon overgrowths. The external morphology and internal zoning of overgrowths on leucosome

and melanosome zircons is similar to that observed in magmatic zircon (Corfu et al. 2003).

In leucosome sample 107-1L (or "1L"), zircon grains are 80-200 μm in length. The cores of the zircons are anhedral to subhedral (Fig. 5A). It is not apparent whether the cores first became rounded through physical abrasion in a detrital setting or chemical dissolution during early stages of anatexis. The cores produced bright CL images, which are typically attributed to lower uranium contents (Nasdala et al., 2003), and they exhibit very little zoning. Overgrowths generally produce darker CL images, indicating higher uranium (as well as other trace elements) contents. This relationship between CL brightness and U content was confirmed by the SIMS data discussed below. The overgrowths are typically euhedral with euhedral oscillatory zoning, defined by alternating lighter and darker CL bands that outline the internal, euhedral shape of zircon growth stages. The CL images show evidence of at least two generations of growth zoning visible, where some inner growths show evidence of resorption, such as truncated tips (Fig. 5A, grain i) or embayments that cross-cut internal zoning (Fig. 5A, grains a, b). These features suggest that growth was interrupted by one or more episodes of dissolution, followed by additional zircon growth.

Zircon grains from melanosome sample 107-1M (or "1M") are slightly different than those from other samples (Fig. 6A). Grain length is approximately 120-200 μm. There are cores and overgrowths in these zircons, as in its companion leucosome (1L) grains, but the cores are only slightly brighter in CL than the surrounding overgrowths, and not nearly as bright as in the cores of the leucosome zircons. The cores are anhedral to subhedral and show internal convolute zoning. External crystal shapes of overgrowths and internal overgrowth zones exhibit euhedral to subhedral shapes. Some overgrowths are unzoned and dark (Fig. 6A, grains a), while others have oscillatory (alternating lighter and darker) zoning (Fig. 6A, grains f, j). Inner growths have truncated tips (Fig. 6A, grain a) and embayments (Fig. 6A, grains a, r). Grain "a" shows an unusual embayment, which penetrates into the convolute core.

In leucosome sample 107-4L (or "4L"), zircon grains are 40-120 μm in length. Cores produce bright CL images, are anhedral to subhedral and have little to no internal zoning (Fig. 7A). These zircons show multiple phases of rim overgrowth, with inner growths having embayments (which cut across older overgrowth zones) (Fig. 7A, grain b) or truncated surfaces (Fig. 7A, grain p). The truncated zircon is surrounded by another generation of growth. The overgrowths are predominantly darker in CL than the cores, an exception being Figure 7A, grain q, which has a very bright outermost rim. Overgrowths are subhedral to euhedral and both oscillatory zoned and dark, unzoned growths are visible.

In melanosome sample 107-4M (or "4M") individual zircons range in size from 90-150 μm. Cores are anhedral to subhedral and produce bright CL images and exhibit little to no zoning (Fig. 8A). Overgrowth rims are darker in CL than the cores, while some overgrowths show oscillatory zoning outlined by lighter CL bands (Fig. 8A, grains n, r). Overgrowths are subhedral to euhedral, as shown by external crystal shapes and internal zonation. Inner rims have embayments (Fig. 8A, grains j, n, r), with another generation of zircon overgrowing them.

In quartzite paleosome sample 107-4Q (or "4Q") zircons are 80-130 μm and they have anhedral cores that produced bright CL images (Fig. 9A). Most cores show irregular edges with slight embayments (Fig. 9A, grains a, b, d). These zircons show a lower volumetric proportion of overgrowth than the other samples, and therefore many are too narrow to analyze. The overgrowths produced darker CL images and are mostly subhedral, with a few grains exhibiting euhedral oscillatory zoning (Fig. 9A, grain x).

5.3 U-Pb Geochronology

Points for SIMS spot analysis were selected from inner zircon cores and outer zircon overgrowth zones visible in CL images (Fig. 5A, Fig. 6A, Fig. 7A, Fig. 8A, Fig. 9A). A table of U-Pb dates and Th/U ratios is provided for all analyses (Table 2). Uncertainties in the tables are

reported at 1 sigma, all uncertainties in the text are reported at 2 sigma. Sample ages will be

addressed in two ways: (1) by evaluating ages within individual samples (Figs. 5-9) and (2) as age

groupings across the five samples (Figs. 10-13) in Section 5.4. Table 3 gives a quick reference as

to which ages are recorded in each sample. Terra-Wasserburg plots with all spot analyses from

each sample are used to illustrate age distributions for both zircon cores and overgrowths in

each individual sample (Fig. 5B, Fig. 6B, Fig. 7B, Fig. 8B, Fig. 9B). Analyses that gave Phanerozoic

ages (overgrowths and convolute cores) are reported as $^{238}U/^{206}Pb$ dates, while U-Pb concordia

plots were used for age assessment of Proterozoic cores.

 The Terra-Wasserburg plot for leucosome sample 1L clearly shows two Phanerozoic

populations for zircon overgrowths (one Cretaceous and one Eocene), as well as a Proterozoic

component documented in the cores (Fig. 5B). Intercept ages calculated using common Pb

values yield ages essentially identical to $^{238}U/^{206}Pb$ ages reported in Table 2 for these samples.

Grain "d" does not reveal a Proterozoic core, but this is attributed to a larger zircon not being

polished deep enough to expose the central core of the grain (Fig. 5A).

 Melanosome sample 1M has only Phanerozoic ages (unlike the other samples, the

convolute cores in this sample were not Proterozoic in age) and are grouped distinctly into two

subsets on a Terra-Wasserburg plot, one Cretaceous in age and the other Eocene (Fig. 6B). The

Cretaceous grouping also consists of three subsets: slightly older convolute cores (colored

brown on the Terra-Wasserburg plot), the first generation of new-growth rims (colored green),

and three analyses which are determined to be "spot-overlap"; that is, part of the mass

spectrometer's ion beam overlapped and analyzed two age domains. This was apparent once

the zircons and U-Pb dating ion beam pits were examined on a petrographic microscope (in both

transmitted and reflected light) where the size of ion pits relative to zircon crystal size and shape

allowed recognition of spot overlap problems. All Eocene analyses for sample 1M are

concordant, whereas some Cretaceous data points show slight discordance. The two most

notable discordant analyses are in the convolute cores. The first, h1, appears to have common

Pb contamination, and the other, r1, is reverse discordant.

The Terra-Wasserburg plot of leucosome sample 4L shows Proterozoic cores and

Cretaceous overgrowth ages, but no documented Eocene ages (Fig. 7B). There are seven

analyses that were determined to result from analytical spot-overlap. The shapes and sizes of

the new-growth zircon rims made getting a clean spot for accurate dating very difficult. The

single remaining new-growth analysis from sample 4L is concordant and dated at 72.9 ± 3.5 Ma.

The Terra-Wasserburg plot for melanosome sample 4M shows a tight cluster of analyses

with Eocene overgrowth dates, as well as scattered, discordant Proterozoic core ages (Fig. 8B).

The e2 spot analysis (with an age of 88.8 ± 5 Ma) is discordant, and is an analytical spot-overlap

between the Proterozoic and Phanerozoic age domains.

The quartzite paleosome sample 4Q Terra-Wasserburg plot has five concordant and

three discordant Proterozoic analyses and one concordant Eocene data point. Three analyses

(f1, k1 and m2) are analytical spot-overlap between these two age groups suggesting a narrow

Eocene overgrowth on these paleosome cores (seen in most of the zircon grains in Fig. 9A).

5.4 Collective Evaluation of Geochronology

The Phanerozoic overgrowth ages (excluding 1M convolute core analyses as well as

those data points which were interpreted as analytical spot-overlap ages) can be grouped into

three populations (Fig. 10; Table 4). The oldest group (designated K, n=15) appears to represent

a single-age population of 70.6 ± 2.6 Ma (Fig. 11). The K age group analyses are from samples 1L

(n = 9), 1M (n = 5) and 4L (n = 1). The MSWD value for this data set is 1.5, just below the

maximum value for a statistically valid population at n = 15 (maximum MSWD = 1.784, Wendt

and Carl, 1991). The second group (designated E1, n=7) is also a single-age population at 45 ±

1.3 Ma (Fig. 12) with an MSWD of 0.36 (for n = 7 the maximum MSWD for a statically valid age is

2.265, Wendt and Carl, 1991). The E1 ages are all from overgrowths in sample 4M, except one

analysis from sample 4Q. The youngest group of zircon ages (designated E2, n=8) includes ages

spanning from 41.8 ± 2.6 Ma to 31.9 ± 1.8 Ma (Fig. 13) and comes from overgrowths in samples

1L and 1M.

Most dates from the Proterozoic cores are discordant. In order to extrapolate a

crystallization age from these analyses, a lower intercept was pinned at 70 Ma, which is the age

assigned to the K group. This Cretaceous event resulted in regional migmatization which

potentially resulted in Pb loss in the existing Proterozoic zircons' U-Pb. A variety of chords from

this 70 Ma lower intercept fit the discordant ages, which lie between 1.0 Ga and 1.8 Ga (Fig. 5D,

Fig. 7C, Fig. 8D, Fig. 9C).

The cores from sample 1M (with convolute zoning) show no Proterozoic inheritance, as

all analyses are concordant at approximately 140 Ma (the exception being one reverse

discordant analysis at 158 Ma). Convolute cores are interpreted as a product of coupled

dissolution-recrystallization, a process where zircon concurrently dissolves and recrystallizes in

the presence of an aqueous metamorphic fluid (Vavra et al., 1998; Corfu et al., 2003). The four

concordant ages yield a weighted mean age of 139.8 ± 6.9 Ma (2σ) with a MSWD of 0.01

(maximum MSWD for a statically valid age at n = 4 is 3.0, Wendt and Carl, 1991). This 140 Ma

age likely represents the age of zircon recrystallization (formation of the convoluted zoning).

Each sample has growth rims from at least one of the three Cretaceous and Eocene

subsets discussed above. Samples 1L and 1M show rim growth from K and E2, but not the 45 Ma

E1 group. One spot analysis from sample 4L falls into the K group, but there are no analyzed

Eocene dates from this sample. Sample 4M has overgrowths dated in the E1 group. Sample 4Q

has only three dated overgrowths and of those, only one was concordant, placing it in the E1 group.

5.5 Th-U Chemistry of Zircons

Zircon cores have fairly low U contents, from 77 ppm to 1200 ppm. However, the new-growth rims have much higher U contents (920 ppm to 7900 ppm). High U contents suppress CL brightness (Nasdala et al., 2003) and this is reflected in the images (Fig. 5A, Fig. 6A, Fig. 7A, Fig. 8A, Fig. 9A). The cores that are Proterozoic in age are much brighter than Phanerozoic overgrowths because of the lower amount of U. The exceptions are cores in sample 1M, which are Phanerozoic in age and have higher U contents relative to cores in other samples. The Th values for zircon cores and rims are similar. Zircon cores have Th values ranging from 19 ppm to 300 ppm. The overgrowths have Th values ranging from 9.2 ppm to 280 ppm.

The Th/U ratios in the Proterozoic cores (Fig. 14) fall between 1 and 0.1 (two analyses fall slightly below 0.1) which is the typical range for igneous zircon (Hoskin and Schaltegger, 2003). In general, Phanerozoic overgrowths have Th/U ratios less than 0.1. Samples in the K group appear to have no consistent Th/U ratio, ranging from 0.1 to nearly 0.001. The Th/U ratios from E1 samples are tightly clustered at about 0.03 and E2 samples fall below the 0.01 line. The Phanerozoic cores from sample 1M fall at or below a Th/U ratio of 0.01, which is indicative of metamorphic zircon (Hoskin and Schaltegger, 2003).

There is a wide variance in Th/U ratios in the zircon cores, from 1.0 to less than 0.01 (Fig. 15). The Th/U ratios in cores from sample 1L are all around 0.5. The Th/U ratios of 4L and 4M cores range from approximately 0.1 to 0.5. Cores from sample 4Q fall between 1 and 0.1. All of the Th/U ratios for zircon overgrowths fall at or below 0.1 (Fig. 16), which is the typical range for metamorphic zircon (Hoskin and Schaltegger, 2003). Leucosome sample 1L analyses plot from 0.1 to below 0.01. Analyses from melanosome 1M and leucosome 4L cluster between 0.01

and 0.001. Analyses from melanosome sample 4M follow a trend around 0.05. The one Th/U

overgrowth analysis from paleosome sample 4Q shows the same value as the 4M samples at

approximately 0.05.

CHAPTER 6: GEOCHRONOLOGY INTERPRETATIONS

There is a clear age division between Proterozoic analyses (dating from 1.8 Ga to 1.0 Ga) and Phanerozoic analyses (dating from 70.6 Ma to 31.9 Ma). Within the Phanerozoic data set (Fig. 10), there is an age gap between the Cretaceous (K) and Eocene age groups (E1 and E2). Based on external morphology and internal zoning of overgrowths on leucosome and melanosome zircons these ages are interpreted to represent growth from a silicate melt. The Cretaceous group of analyses is interpreted as a single-age population at 70.6 Ma. Fourteen of the fifteen analyses in the K age population are overgrowths on zircon from a contiguous leucosome-melanosome pair (1L-1M). Some Cretaceous growth zones are truncated by dissolution surfaces that are surrounded by additional zircon overgrowths, some belonging to the K age population and others belonging to the E2 age population. Thus, zircon growth was interrupted by zircon dissolution at least during Cretaceous zircon crystallization. E1 also is interpreted as a single-age population at 45 Ma. Six of seven analyses in the E1 population (Fig.12) are from zircon overgrowths from melanosome sample 4M, the remaining analysis is from the contiguous paleosome sample (4Q). The third set is a range of ages spanning 41.8 Ma to 31.9 Ma; all of these ages are from one contiguous leucosome-melanosome pair (1L-1M) and mantle Cretaceous (K) overgrowths including dissolution features truncating K zircon growths (Figs. 5A, 6A , 11, 13) . Based on the weighted mean ages for K and E1, there is a 25 Ma gap in zircon growth between the Cretaceous and Eocene.

Questions that need to be addressed in this project are mainly concerned with the wide spread of Cretaceous and Eocene ages, and whether or not the age range seen in the Eocene (E2) data set is real. There are three different possibilities regarding the E2 age span. It can be interpreted as (1) a real age gradient, (2) a single-age population that has undergone Pb loss or

22

(3) the analyses have minor amounts of spot-overlap that weren't immediately obvious during data analysis.

6.1 Real Age Range Hypothesis

The first interpretation to be considered is that the E2 subset is a real age gradient from 41.8 Ma to 31.9 Ma. In this scenario, no significant Pb loss has occurred, and the ages obtained have real geologic meaning. The remaining two interpretations of the Eocene ages conclude that there is no real age gradient.

6.2 Pb Loss Hypothesis

In the instance of interpretation 2, the oldest age (45 Ma) is interpreted as the true age of crystallization and the younger zircon grains lost Pb. This means that the bulk of the Eocene zircon overgrowths was open to Pb loss and closed at approximately 31.9 Ma.

Some major causes of Pb loss include radiation damage due to high U concentrations and interaction with hydrothermal fluids. No recrystallization textures associated with fluid interactions were present. Radiation damage could be responsible for the Pb loss seen in these zircons, but it is important to recognize that radiation damage is a function of both U content and time. The higher the U content and the longer it's left to decay, the more likely damage is to accumulate, causing the grain to become susceptible to Pb loss.

Looking at the distribution of U in the Eocene zircon rims (Fig. 16), problems with the Pb loss interpretation can be seen. The E1 zircon overgrowths have some of the highest U concentrations of the data set (Fig. 16), and represent a single-age event at 45 Ma. Most of the E2 group has the same U concentration as E1, yet is interpreted as an age gradient between 41 Ma and 31 Ma. If the Eocene zircons had experienced Pb loss, then it is expected that E1 and E2 ages would be the same. There is also a small portion of the E2 data set which has much lower U

than the rest of the E2 or E1 group. These grains should be less susceptible to Pb loss, and

therefore document an older age, but they are younger than the E1 45 Ma age.

In further opposition to the Pb loss interpretation, the inherited Proterozoic zircon cores

found in all samples (besides 1M) have had substantial time to accumulate radiation damage,

yet some of them are still concordant. Furthermore, melanosome sample 1M has cores with

convolute textures and ages around 140 Ma (except for one reverse-discordant analysis at 158

Ma). These zircon cores have some of the highest U content of any of the samples (Fig. 14, Fig.

15), yet all of the analyses are concordant. If the overgrowths are interpreted as being reset due

to radiation damage, then these older, higher U content zircons should also be reset and that is

not observed. So even with the higher U content seen in the Phanerozoic zircon, it doesn't seem

plausible that 10 Ma is enough time to accumulate radiation damage.

6.3 Spot-Overlap Hypothesis

The third interpretation to explain the age spread in the Eocene data set is that the age

range represents spot-overlap. If this were the case, then the real Eocene crystallization age is

31.9 Ma, and the older age analyses are due to analyzing small amounts of the older zircon

cores or overgrowths. As noted in chapter 5.3, data points with obvious mixing lines on the

Terra-Wasserburg plots have been excluded from the data set.

Applying interpretation 3 to the E2 age span, Th/U ratios were compared between the

E2 overgrowths and their cores (from samples 1L and 1M) (Fig. 17). The Proterozoic cores are

distinct from the E2 overgrowths, but the E2 overgrowths and 1M cores had very similar ratios.

There's a possibility that spot analysis a3 might have contamination from the convolute core,

but spots a4 and a5 don't appear to be close enough to the core to have experienced

contamination (Fig. 6A). The remaining two analyses that surround 1M cores are spots f2 and f3.

Again, neither seems close enough to be contaminated from the convolute core. All of the E2

analyses have approximately the same Th/U ratios. The Proterozoic cores generally have lower

Th/U ratios than the Phanerozoic analyses (Fig. 14); therefore the similarity of E2 and 1M core

data is attributed to broadly similar Phanerozoic Th/U ratios. In light of rejecting spot-overlap

for the E2 subset of data, the conclusion can be drawn that this third interpretation is not

supported by substantial evidence.

6.4 Geochronology Interpretation Conclusion

It thus seems most likely that the E2 age range represents a real continuum of

migmatite crystallization. This means that there was an approximately 10 Ma period of partial

melting in the Eocene. While this is a long timeframe for migmatization to be active, protracted

melt events have been documented elsewhere. Kruckenberg et al. (2008) documented

migmatization in a part of the northern Cordillera that spanned 12 Ma, and Hermann and

Rubatto (2003) documented a 20 Ma granulite-facies migmatite event in northern Italy.

Recently, Howard et al. (2011) conceded that evidence points to multiple instances of long

periods of successive or rejuvenated igneous crystallization in the Ruby Mountains-East

Humboldt Range complex. Howard et al. (2011) used SHRIMP dating of both monazite and

zircon from pegmatitic leucogranite in the Ruby Mountains, and obtained very similar spread of

ages to those reported in this study. Figure 9 of Howard et al. (2011) graphically represents the

range of ages seen in the monazites and zircons, showing a spread of ages from approximately

45 Ma to 25 Ma. Given these findings, the 10 Ma Eocene age range appear geologically

plausible.

CHAPTER 7: DISCUSSION

7.1 Implications for Protolith

An important component of this project was finding and dating in-situ generated melts (as opposed to a magma injection age) and used to date cooling from the metamorphic thermal peak. The samples used in this study were collected from a single map unit (CZqs in Fig. 2) defined as quartzite (paleosome) and schist (melanosome) and leucogranite gneiss (leucosome). The ZCqs unit is interpreted as meta-clastic rock (quartz-rich sandstone and argillite) of Neoproterozoic to Cambrian age (Lush et al., 1998; Henry et al., 2011). In order to assess whether the melt was locally-sourced and non-mobile (a requirement for dating metamorphism at the exposure level), ages from the Proterozoic zircon cores from the quartzite paleosome (sample 4Q) were compared with zircon core ages of the leucosomes and melanosomes from the rest of the samples (1L, 1M, 4L and 4M). The hypothesis is that leucosome and melanosome generated during partial melting of CZqs metasedimentary protolith package should have similar inherited detrital zircon ages to that found in the quartzite paleosome. The paleosome is thought to have had minimal interaction with melt during migmatization, and should represent the detrital zircon ages of the CZqs unit as a whole (including meta-clastic protoliths that generated leucosome and melanosome).

Many of the Proterozoic core ages are discordant, so to determine the inheritance ages, a lower intercept of 70 Ma was chosen as an age for Pb loss. This age was chosen because a substantial amount of zircon grew in the migmatites during this time, indicating high temperatures and anatexis. Chords were plotted from the 70 Ma lower intercept to determine upper intercept (or inheritance age). Zircon cores from samples 1L, 4L, 4M and 4Q show a wide variety of inheritance ages, from 1800 Ma to 1000 Ma, when plotted on a concordia diagram

(Fig. 5D, Fig. 7C, Fig. 8D, Fig. 9C). The only sample whose cores were not plotted on a concordia diagram was melanosome sample 1M because those zircons do not have Proterozoic cores (Fig. 6D).

Cores from the quartzite paleosome sample 4Q have upper intercepts between 1000 Ma and 1800 Ma (Fig. 9D). There are eight 4Q core analyses, three of which are discordant. There are four nearly concordant analyses and one analysis that is concordant. Cores from leucosome sample 1L have upper intercepts around 1400 Ma (Fig. 5D). Two of the three 1L core analyses were discordant, with the third being nearly concordant. Leucosome 4L cores have upper intercepts between 1000 Ma and 1600 Ma (Fig. 7C). All five of these analyses were discordant. Melanosome 4M cores have upper intercepts between 1000 Ma and 1800 Ma (Fig. 8D). Five of the ten 4M core analyses were discordant, three were nearly concordant and two were concordant.

While this analysis does not involve the large populations and rigorous statistical treatment typically applied in detrital zircon studies, the similarity of Proterozoic zircon cores between the paleosome sample (4Q) and three of four leucosome-melanosome samples (1L, 4L, 1M) are consistent with a common provenance and does support the interpretation that new growth zircon (K, E1 and E2 ages) grew from in situ melts. In addition, the spread of potential upper intercept (and some concordant) ages recorded in the zircon cores is also consistent with the Neoproterozoic to Cambrian protolith age assigned to these rocks by Lush et al. (1988) and Henry et al. (2011).

The convoluted cores in melanosome sample 1M represent a unique inheritance relative to the other samples and their interpretation proves challenging as they don't record the same Proterozoic inheritance as their (presumed) leucosome counterpart (1L). Instead of discordant Proterozoic dates, these 1M zircon cores have concordant dates at approximately

140 Ma surrounded by K and E2 new-growth rims (Fig. 6D) similar in age to those of the

adjacent leucosome 1L (Fig. 5D). A possible origin of the 140 Ma convoluted core may be found

in a Late Jurassic amphibolite facies dynamothermal metamorphic event recorded in the Ruby

Mountains that included emplacement of a suite of 152 ± 1 Ma two-mica granites (Hudec and

Wright, 1991; Hudec, 1992). One possible explanation for the 140 Ma convoluted cores is that

the protolith for melanosome 1M was a late Jurassic to Early Cretaceous two-mica leucogranite

dike or sill that crystallized zircon, which then underwent coupled dissolution reprecipitation as

the rock cooled through subsolidus temperatures and was exposed to aqueous fluids released

by the crystallizing leucogranite magma.

   If the cores from sample 1M are from a dike injection, then this sample would not be

the melanosome restite generated by extraction of1L leucosome melt; instead melanosome 1M

is the restite left behind by a melt that mobilized beyond the outcrop scale. . This has important

sampling implications for any future work. The samples collected for this study are stromatic

migmatites, so it is presumed that leucocratic bodies and adjacent biotite-rich melanosomes are

genetically related. The inherited zircon cores of these rocks clearly demonstrate that their

protoliths are not genetically linked.

7.2 Implications for Migmatization

   Another important piece of information that can be gleaned from this investigation

relates to the distribution of new-growth zircon in migmatites. As discussed earlier, the

deformation-assisted melt segregation (DAMS) model predicts that the melanosome should

contain inherited zircon, while the leucosome should have new growth zircon that crystallized

from the melt. However, the CL images from the EHR migmatite zircons demonstrate abundant

new growth on the melanosome zircon as well as the leucosome zircon. Voluminous

overgrowths on zircon cores have also been reported from melanosome zircons in migmatites of the Ivrea zone (Vavra et al., 1996, 1999). The paleosome samples also show thin rims of new-growth zircon which suggests small percentages of grain boundary melts even in the paleosomes. Thus it appears that melt permeated all parts of the migmatite. If this process is common then a revised melt-solid segregation model may be needed, one where melt segregation is less efficient.

As previously discussed, what might be considered a leucosome-melanosome pair due to contact relationships seen in the field could in fact be two rocks from unrelated protolith sources. Sample 107-1 is a good example of this issue. The leucosome (1L) has inherited Proterozoic zircon cores, while the contiguous melanosome (1M) has cores that are Early Cretaceous in age. While it is clear that these two rocks are from different protoliths, they record the same melting events. Both 1L and 1M zircons show evidence of zircon crystallization that records K and E2 melting events, which is expected because of the spatial relationship between 1L and 1M. It is reasonable for two rocks that are adjacent to each other to record the same melting events.

A question that remains to be answered is how the leucosomes and melanosomes of the samples record growth from different melting events. From sample 107-4, the 4L leucosome documents K zircon growth, while the 4M melanosome only has zircon growth from the E1 event. The leucosome came in contact with the Cretaceous melting event, yet the melanosome is only involved in the first Eocene melt. It is unclear how these melting events could appear so localized as to bypass adjacent lithologies, yet are so widespread within the core complex. It is apparent that the part the melanosome and paleosome plays in the migmatitic system is poorly understood and needs to be further studied.

7.3 Implications for Core Complex Evolution

This section will look at how the East Humboldt Range metamorphic core complex evolved during tectonically active periods in the Mesozoic and Cenozoic. Assuming that the Phanerozoic data set is interpreted as geologically meaningful ages, then the ages obtained represent times of crystallization of zircon in migmatite melts. The new growth zircon surrounding the inherited cores shows evidence for two zircon crystallization events (Fig. 10) – one in the Late Cretaceous (70.8 Ma, Fig. 11) one in the Eocene, as well as evidence of dissolution during the Late Cretaceous event. The Eocene event has been subdivided into the Eocene E1 and E2 events (recorded in zircons from different samples); the earlier E1 (45 Ma, Fig. 12) is single-age population largely from a single sample (Fig. 8) and followed by a protracted growth event (41.8 to 31.9 Ma; Fig. 13) recorded in two contiguous samples where E2 zircon overgrows K-age zircon (Figs. 5 and 6). Below the results of this study are integrated with previous data and interpretations regarding the evolution of the RM-EHR metamorphic core complex (see Fig. 19).

The EHR lies in the hinterland of the Sevier orogenic belt, farther west than the main frontal thrust belt. DeCelles (2004) brackets thrusting during the Sevier orogeny to between 155 Ma and 55 Ma. Sevier-related compressional deformation in near the EHR is inferred on the Windermere thrust (Camilleri and Chamberlain, 1997). McGrew et al. (2000) used new and published thermobarometry results for the Winchell Lake nappe in EHR to construct a clockwise P-T-time path with a thermal peak of 800°C at 9 kbars in Late Cretaceous followed by Cenozoic cooling and decompression to 630°C and 5 kbars. An 84.8 Ma (^{207}Pb/^{206}Pb TIMS) leucogranite in the hinge zone of the Winchell Lake nappe (Fig. 19) is interpreted as an anatectic melt that migrated from the fold limbs during nappe emplacement related to Sevier-age thrusting; the

age records melt crystallization as the complex cooled from the thermal peak (McGrew et al. 2000). The 70.8 Ma Late Cretaceous (K) age reported here records crystallization of an in-situ anatectic melt following cooling from the thermal peak but this age is from the lower limb of the Winchell Lake nappe. The 15 Ma difference in ages from the hinge and lower limb of the nappe (Fig. 19) may reflect later cooling in deeper parts of the complex, anatectic melts of different compositions with different solidus temperatures, or a combination of both. Premo et al (2008) reported a spread of U-Pb zircon overgrowth ages (with Archean cores) between 91 and 72 Ma ($^{238}U/^{206}Pb$ SIMS) from a single migmatite sample from core of the Winchell Lake nappe (Fig. 19). These zircon overgrowths are thought to record crystallization of anatectic melt (Premo et al., 2008, 2010; McGrew and Snoke, 2010) but the interpretation of these ages is problematic. Premo et al. (2008) interpreted the age spread as resulting from Pb loss from ~90 Ma high U zircons with younger ages representing lead loss that closed at ~70 Ma. Alternatively these ages could reflect 70 Ma zircon growth with older ages resulting from spot overlap with Archean cores.

Wells and Hoisch (2008 and references there in) have documented periods of syn-convergent Late Cretaceous extension in a number of Cordilleran metamorphic core complexes in the hinterland of the Sevier orogenic belt. If the 15 Ma difference in migmatite crystallization ages from the hinge and lower limb of the Winchell Lake nappe represent cooling ages, it may mark the onset of a Late Cretaceous extensional collapse of the over thickened crust in the EHR. The Cordilleran belt of metamorphic core complexes is coincident with a belt of Late Cretaceous to Eocene peraluminous granite plutons (Miller and Bradfish, 1980; Wells and Hoisch, 2008) and includes numerous small leucogranite bodies emplaced into the Ruby Mountains portion of the RM-EHR core complex between 92 – 29 Ma (Howard et al., 2001). Potential thermal drivers for this episode of middle crustal high grade metamorphism and peraluminous plutonism include

injection of mantle-derived mafic magmas into the lower crust (Lee et al., 2003) and increased

mantle heat flow into the crust as a result of lithospheric delamination (Wells and Hoisch, 2008).

^{40}Ar/^{39}Ar data from EHR hornblende yields cooling ages of 36-29 Ma at deep structural

levels and 65-49 Ma at shallow structural levels and mica (muscovite and biotite) cooling ages of

27 to 21 Ma at all structural levels (McGrew and Snee, 1994). The ^{40}Ar/^{39}Ar cooling ages are

thought to record extensional uplift and unroofing of the EHR metamorphic complex (McGrew

and Snee, 1994; McGrew et al., 2000). The Eocene ages reported here, E1 at 45 Ma and E2

between 41.8 and 31.9 Ma, appear to record zircon crystallization during a second protracted

anatectic migmatization event during this period of uplift (Fig. 19). Based on U-Pb dating of

monazite and zircon, it was determined that emplacement of quartz diorite to leucogranite

magmas occurred between 40 and 29 Ma and that mylonitization of those plutons occurred

between 29 and 23 Ma (Wright and Snoke, 1993). Thus, the E1 (45 Ma) and E2 (41.8 to 31.9 Ma)

events were likely triggered by heat advection of magmas from depth during extension (and

core complex unroofing) (Fig. 19). Local injections of melt may have been responsible for the

continued migmatization and zircon growth. The heat input from injected magmas, particularly

more mafic quartz diorite, may have raised temperatures locally enough to generate small

volumes of partial melt, and then cooled below the solidus in a short time frame. If melt

injection was repetitive, as it appears to be based on Wright and Snoke's 11 Ma interval of

pluton emplacement (Wright and Snoke, 1993), then it may have been possible to produce

repeated melting and crystallization events over a protracted period of time.

CHAPTER 8: CONCLUSIONS

This study adds to the body of evidence supporting Cretaceous thrust burial and Eocene unroofing of the East Humboldt Range in northern Nevada. Zircons separated from migmatites of the Winchell Lake nappe record two migmatization events separated by 25 Ma, one in the Cretaceous and the other in the Eocene. The Cretaceous event is a single pulse of migmatization dated at 70 Ma. This correlates with U-Pb dates of zircons and monazites within the EHR by McGrew et al. (2000), Premo et al. (2008) and Howard et al. (2011). Two generations of Eocene zircon growth are documented. The first is a single age of 45 Ma, and the second growth is a range of ages from 41 Ma to 31 Ma. Eocene ages are also supported by data from Howard et al. (2011). Ages of inherited cores of the migmatite zircons agree with previous interpretations of a Neoproterozoic protolith (McGrew, 1992; Lush et al., 1988), while the convolute cores of sample 1M most likely crystallized from Jurassic dike injections (Hudec, 1990).

In addition to geochronology findings, it was determined that genetic relationships cannot be easily inferred from field relationships. Samples 1L and 1M were assumed to be linked (1M being the site of melt extraction and 1L being the site of melt accumulation), but they have different inherited zircon ages. Despite not being a leucosome-melanosome pair, they both subsequently record the Cretaceous and Eocene melting events.

Finally, it has been determined that whereas we have a basic understanding of migmatite formation, the details of melt segregation are poorly understood. According to the widely-accepted DAMS model, zircon should only crystallize in the leucosome, however there is abundant growth in melanosome zircons, and even some in the quartzite paleosome. Further experimentation is needed to better constrain the physical and chemical components of melt segregation.

Appendix 1: Tables and Figures

Table 1. Locations of Sampled Migmatites

Sample Number	Latitude (°N)	Longitude (°W)	Elevation (m)
107-1	41°01'23.8"	115°05'27.1"	2680
107-4	41°01'25.0"	115°05'19.1"	2607

TABLE 2. Analyses Grouped by Sample

Analysis	238U/206Pb	±	207Pb/206Pb	±	204Pb/206Pb ×1000	±	Correlation of TW Concordia Ellipses	206Pb/238U age [Ma]	±	207Pb/206Pb age [Ma]	±	Th/U	U ppm	Th ppm	%206Pb*	U/U*
107_1L_a1	87.1	6.4	0.0494	0.0029	0	0	0.01	73.5	5.4		*	0.093	1,500	140	8.0	99.8
107_1L_a2	13.4	0.7	0.0769	0.0025	0.139	0.0922	0.14	454	25	1,070	80	0.23	590	140	8.5	97.3
107_1L_a3	103	7	0.0489	0.0014	0.166	0.0858	0.02	622	39	*	*	0.0028	3,200	9.2	7.9	99.8
107_1L_b1	6.44	0.68	0.0835	0.0015	0.0696	0.0618	-0.01	914	92	1,260	40	0.49	170	84	7.8	98.2
107_1L_b2	87.3	5	0.0489	0.0019	0.339	0.175	0.10	73.4	4.2	*	*	0.09	1,200	110	8.1	99.8
107_1L_b3	153	10	0.0522	0.0025	4.5	0.749	0.10	41.8	2.8	*	*	0.0049	1,800	8.7	8.0	99.3
107_1L_d1	95.3	4.4	0.0487	0.0009	0.0753	0.0435	0.03	67.2	3.3	*	*	0.0045	3,800	17	8.4	99.8
107_1L_d2	162	11	0.0459	0.0031	0.219	0.167	-0.14	39.9	2.7	*	*	0.0095	2,000	17	7.9	100.1
107_1L_d3	183	8	0.0494	0.0019	0.106	0.106	-0.01	35.1	1.7	*	*	0.0083	1,600	13	8.5	99.7
107_1L_i1	4.79	0.4	0.0915	0.0021	0	0	0.14	1,205	92	1,457	44	0.26	83	22	8.1	98.5
107_1L_i2	87.7	4.4	0.0477	0.0014	0.131	0.0937	0.03	73.1	3.6	*	*	0.01	1,900	20	8.3	100.0
107_1L_i3	94.7	4.6	0.0484	0.0012	0.14	0.0683	-0.02	67.7	3.3	*	*	0.0036	3,200	11	8.4	99.9
107_1L_l1	78.7	6	0.0526	0.002	0.35	0.194	-0.05	81	6.1	*	*	0.019	1,200	24	7.7	99.4
107_1L_l3	90.8	4.5	0.0514	0.0014	0	0	0.05	70.3	3.5	*	*	0.11	1,500	170	8.4	99.5
107_1L_l4	79.2	3.8	0.0476	0.0019	0.179	0.127	0.02	80.9	3.9	*	*	0.071	920	65	8.4	100.0
107_1M_a1	45.9	2.2	0.0497	0.0006	0.0123	0.0109	-0.01	139	7	*	*	0.0078	5,200	40	8.3	99.9
107_1M_a2	60	2.9	0.0497	0.0008	0.136	0.0523	0.01	106	5	*	*	0.0056	3,300	18	8.3	99.8
107_1M_a3	189	10	0.0488	0.0009	0.151	0.0713	-0.02	34.2	1.7	*	*	0.0054	6,800	37	8.2	100.0
107_1M_a4	202	11	0.0486	0.0016	0	0	-0.05	31.9	1.8	*	*	0.0042	5,700	24	8.1	99.8
107_1M_a5	174	8	0.0466	0.0009	0.131	0.0586	0.01	37	1.8	*	*	0.0049	6,900	34	8.3	100.0
107_1M_f1	45.7	2.2	0.0492	0.0009	0.0405	0.0181	0.01	140	7	*	*	0.0053	5,800	31	8.4	99.9
107_1M_f2	178	9	0.0492	0.0012	0.23	0.0629	-0.03	36.2	1.8	*	*	0.0036	6,400	23	8.3	99.7
107_1M_f3	164	8	0.0497	0.0013	0.0651	0.046	-0.02	39.2	1.9	*	*	0.0033	5,300	18	8.3	99.6
107_1M_h1	45.4	2.2	0.0514	0.0006	0.0676	0.0229	0.03	140	7	*	*	0.011	7,300	83	8.4	99.7
107_1M_h2	92.5	5.4	0.0499	0.001	0	0	0.01	69.2	4	*	*	0.0036	4,400	16	8.0	99.7
107_1M_j1	84.7	4.9	0.0499	0.001	0.0236	0.0236	0.00	75.5	4.4	*	*	0.0034	5,000	17	8.0	99.7
107_1M_j2	72.2	3.8	0.0494	0.0011	0.161	0.0721	0.02	98.8	4.7	*	*	0.01	2,800	28	8.1	99.8
107_1M_r1	40.4	1.7	0.0482	0.0002	0.0081	0.0062	0.00	158	8	*	*	0.004	7,700	31	8.6	100.1
107_1M_r2	91.3	4.1	0.0477	0.0019	0.0852	0.0458	-0.04	70.3	3.4	*	*	0.0035	3,500	12	8.4	100.0
107_1M_r3	96.6	4.5	0.0482	0.0011	0.0284	0.0284	0.00	66.3	3.2	*	*	0.0042	5,400	23	8.4	99.9
107_1M_r4	93.9	5	0.0485	0.0011	0.055	0.0317	0.04	68.3	3.6	*	*	0.0046	6,200	29	8.2	99.9
107_1M_p1	45.5	2.2	0.049	0.0008	0.0222	0.0179	-0.04	140	7	*	*	0.0061	3,200	19	8.4	100.0
107_1M_p2	62.2	2.8	0.05	0.0012	0.0573	0.036	-0.05	103	5	*	*	0.0072	2,200	15	8.5	99.8

Analysis	238U/206Pb	±	207Pb/206Pb	204Pb/206Pb *1000	±	Correlation of TW Concordia Ellipses	206Pb/238U age [Ma]	±	207Pb/206Pb age [Ma]	±	Th/U	±	U ppm	Th ppm	% 206Pb*	UO/U+
107_4L_b1	8.33	0.52	0.0976	0.0781	0.059	0.02	699	44	1,560	30	0.25		210	52	8.2	95.4
107_4L_b2	87.9	4.1	0.0488	0.205	0.113	-0.02	72.9	3.5	*		0.0062		1,300	11	8.4	99.8
107_4L_l1	6.31	0.51	0.09	0.0463	0.035	-0.04	925	73	1,410	40	0.38		260	100	8.4	97.3
107_4L_l2	58.5	3.3	0.0507	0.132	0.075	-0.02	10m	6	*	*	0.0054	*	1,500	8.1	8.2	98.7
107_4L_l3	60.7	4.1	0.0485	0.0474	0.055	-0.02	98	5.8	*	*	0.0056	*	1,400	7.5	8.1	99.5
107_4L_k1	8.47	0.52	0.0849	0.0287	0.029	0.07	700	42	1,310	40	0.36		560	200	8.2	97.1
107_4L_k2	5.9	0.41	0.0857	0.115	0.038	0.01	993	85	1,290	20	0.21		700	150	7.9	98.2
107_4L_l1	18.1	0.9	0.0752	0.0332	0.039	-0.03	334	17	1,000	50	0.16		450	75	6.5	97.2
107_4L_l2	64.6	4.6	0.0545	0.197	0.143	-0.03	98.4	7	*	40	0.011		1,500	17	7.6	99.2
107_4L_g1	19.3	1.5	0.0773	0.179	0.088	0.06	316	25	1,060		0.14		1,200	170	7.8	96.8
107_4L_g1	7.05	0.33	0.0733	0.0657	0.029	0.01	849	41	995	29	0.24		490	120	8.5	99.2
107_4L_g2	60.1	5.4	0.0513	0	0	0.05	105	10			0.017		680	15	7.6	99.6
107_4L_g3	22.2	1.3	0.0704	0.00662	0.013	0.04	278	17	939	41	0.1		890	89	6.3	97.6
107_4M_a1	5.58	0.31	0.0792	0.0629	0.063	0.02	1,057	68	1,155	52	0.35		97	34	8.2	99.4
107_4M_b1	4.83	0.31	0.106	0.0574	0.032	0.02	1,173	72	1,720	25	0.3		270	80	8.6	96.4
107_4M_b2	3.43	0.21	0.11	0	0.024	-0.01	1,629	90	1,793	24	0.35		240	85	8.4	98.7
107_4M_d1	9.74	0.45	0.0752	0.0388	0.03	-0.01	619	30	1,060	30	0.44		700	300	8.5	98.1
107_4M_d2	146	7	0.0469	0.0421	0.133	-0.01	44.1	2.2	*	*	0.031		7,600	230	8.3	100.0
107_4M_e1	13.3	0.9	0.093	0.608	0.033	-0.05	444	30	1,300	50	0.24		610	150	8.0	95.2
107_4M_e2	70.3	3.8	0.0676	0.0224	0.03	0.01	98.6	5	843	50	0.044		2,300	100	8.4	97.5
107_4M_h1	5.51	0.38	0.0767	0.0303	0.047	-0.09	1,074	69	1,101	48	0.45		200	91	8.3	99.8
107_4M_j1	9.48	0.43	0.0828	0.0659	0.059	0.06	629	30	1,240	40	0.43		260	110	8.8	97.1
107_4M_j2	136	7	0.0461	0.114	0.054	0.04	47.5	2.5	*	*	0.033		5,300	180	8.2	100.1
107_4M_n1	147	8	0.0456	0.143	0.033	0.00	44	2.4	*	*	0.038		7,100	270	8.1	100.2
107_4M_n2	9.74	0.66	0.123	0.0573	0.027	-0.02	581	41	1,980	20	0.13		520	93	8.4	91.8
107_4M_n3	146	6	0.0494	0.0387	0.028	-0.01	43.8	2.1	*	*	0.032		7,000	68	8.5	99.7
107_4M_q1	3.26	0.3	0.101	0.0276	0.059	-0.03	1,732	140	1,640	27	0.32		160	220	8.0	100.7
107_4M_q2	140	8	0.046	0.121	0.018	0.00	46.1	2.5	*		0.033		6,200	50	8.1	100.1
107_4M_r1	4.07	0.3	0.0916	0.0175	0.043	0.00	1,411	93	1,453	25	0.39		270	200	8.2	99.7
107_4M_r2	146	7	0.0478	0.0858	0.027	-0.03	44.2	2.2	*	*	0.036		7,900	100	8.3	99.9
107_4Q_a1	3.84	0.26	0.0995	0.0233	0.018	-0.01	1,480	90	1,610	20	0.79		120	280	8.4	99.1
107_4Q_b1	10.1	0.5	0.0735	0.0206	0.021	-0.02	596	32	1,020	20	0.25		650	93	8.4	98.2
107_4Q_b2	140	6	0.0469	0.024	0.04	0.02	45.9	2.2	*		0.034		7,000	170	8.4	100.0
107_4Q_d1	12.3	0.7	0.084	0.04	0.036	0.10	485	26	1,280	60	0.27		300	240	8.4	96.5
107_4Q_f1	35	1.8	0.0736	0.036	0.122	0.02	171	9	1,020	40	0.061		1,100	80	8.4	96.9
107_4Q_k1	29.3	1.6	0.0701	0.227	0.075	-0.06	211	12			0.24		450	68	8.5	97.5
107_4Q_m1	7.92	0.8	0.0912	0.173	0.158	0.05	741	55	1,400	40	0.4		290	110	8.2	96.4
107_4Q_m2	37.3	2.4	0.0657	0.542	0.082	0.00	167	11			0.046		1,200	120	7.9	97.7
107_4Q_o1	4.68	0.29	0.0883	0.204	0.113	-0.03	1,240	70	1,325	42	0.37		160	58	8.3	99.1
107_4Q_t1	3.52	0.35	0.107	0.227	0	0.06	1,597	143	1,696	52	0.24		77	57	8.1	98.8
107_4Q_u1	6.57	0.58	0.0711	0	0.051	0.06	911	76	961	41	0.43		95	19	8.0	99.8
107_4Q_x1	5.3	0.43	0.0827	0.0691		0.00	1,105	83	1,239	33	0.78		280	41	8.2	99.2

Table 2. Analytical analyses for migmatite zircons. All spot analyses are included in this table, arranged by sample number. Red data points were determined to be spot-overlap, and have been eliminated so as not to skew any geochronology results.

| Sample	# Dated Cores			# Dated Overgrowths			
	Proterozoic	Jurassic-Cretaceous	Eliminated Analyses	K	E1	E2	Eliminated Analyses
1L	3			9		3	
1M		5		5		5	3
4L	5		2				6
4M	10				6		1
4Q	8				1		3

Table 3. Recorded ages within samples. Age relationships recorded within the five samples. Eliminated analyses are spot-overlap analyses.

TABLE 4. Analyses Grouped by Age

Age Group	Analysis	238U/206Pb	±	207Pb/206Pb	±	204Pb/206Pb x1000	±	Correlation of TW Concordia Ellipses	206Pb/238U age [Ma]	±	207Pb/206Pb age [Ma]	±	±	Th/U	±	U ppm	Th ppm	% 206Pb	U/Th*
E2	107_1M_a4	202	11	0.0466	0.0016	0	0	-0.08	31.9	1.8			*	0.0042	*	5,700	24	8.1	99.8
E2	107_1M_a3	189	10	0.0468	0.0009	0.151	0.0713	0.02	34.2	1.7			*	0.0054	*	6,800	37	8.2	100.0
E2	107_1L_d3	183	8	0.0494	0.0019	0.106	0.106	-0.01	35.1	1.7			*	0.0083	*	1,600	13	8.5	99.7
E2	107_1M_f2	178	9	0.0492	0.0012	0.23	0.0829	-0.03	36.2	1.8			*	0.0036	*	6,400	23	8.3	99.7
E2	107_1M_a5	174	8	0.0468	0.0009	0.131	0.0586	0.01	37	1.8			*	0.0049	*	6,900	34	8.3	100.0
E2	107_1M_f3	164	8	0.0497	0.0013	0.0651	0.046	-0.02	39.2	1.9			*	0.0053	*	5,300	18	8.3	99.6
E2	107_1L_d2	162	11	0.0459	0.0031	0.219	0.157	-0.14	39.9	2.7			*	0.0085	*	2,000	17	7.9	100.1
E2	107_1L_b3	153	10	0.0522	0.0025	4.5	0.749	0.10	41.8	2.6			*	0.0049	*	1,800	8.7	8.0	99.3
E1	107_4M_n3	146	6	0.0494	0.0009	0.0387	0.0273	-0.01	43.8	2.1			*	0.032	*	7,000	220	8.5	99.7
E1	107_4M_n1	147	8	0.0456	0.001	0.143	0.0844	0.00	44	2.4			*	0.038	*	7,100	270	8.1	100.2
E1	107_4M_d2	146	7	0.0469	0.0011	0.0421	0.0298	-0.01	44.1	2.2			*	0.031	*	7,600	230	8.3	100.0
E1	107_4M_f2	146	7	0.0478	0.0011	0.0858	0.0429	-0.03	44.2	2.2			*	0.036	*	7,900	280	8.3	99.9
E1	107_4Q_b2	140	6	0.0469	0.0009	0.024	0.0213	0.02	45.9	2.2			*	0.034	*	7,000	240	8.4	100.0
E1	107_4M_Q2	140	8	0.046	0.0009	0.121	0.0586	0.09	46.1	2.5			*	0.053	*	6,200	200	8.1	100.1
E1	107_4M_f2	136	7	0.0461	0.0012	0.114	0.0588	0.04	47.5	2.5			*	0.033	*	5,300	180	8.2	100.1
K	107_1L_a3	103	7	0.0488	0.0014	0.166	0.0858	0.02	62.2	3.8			*	0.0029	*	3,200	9.2	7.9	99.8
K	107_1M_f3	96.8	4.5	0.0462	0.0011	0.0284	0.0284	0.00	66.3	3.2			*	0.0042	*	5,400	23	8.4	99.9
K	107_1L_d1	95.3	4.4	0.0467	0.0009	0.0753	0.0435	0.03	67.2	3.3			*	0.0045	*	3,800	17	8.4	99.8
K	107_1L_f3	94.7	4.6	0.0484	0.0012	0.14	0.0683	-0.02	67.7	3.3			*	0.0036	*	3,200	11	8.4	99.9
K	107_1M_f4	93.9	5	0.0485	0.0011	0.055	0.0317	0.04	68.3	3.6			*	0.0046	*	6,200	29	8.2	99.9
K	107_1M_f2	92.5	5.4	0.0499	0.001	0	0	0.01	69.2	4			*	0.0036	*	4,400	16	8.0	99.7
K	107_1L_f3	90.8	4.5	0.0514	0.0014	0	0	0.05	70.3	3.5			*	0.11	*	1,500	170	8.4	99.5
K	107_1M_f2	91.3	4.1	0.0477	0.0019	0.0852	0.0458	-0.04	70.3	3.4			*	0.0035	*	3,500	12	8.4	100.0
K	107_4L_b2	87.9	4.1	0.0488	0.0022	0.205	0.113	-0.02	72.9	3.5			*	0.0082	*	1,300	11	8.4	99.8
K	107_1L_f2	87.7	4.4	0.0477	0.0014	0.131	0.0937	0.03	73.1	3.6			*	0.01	*	1,900	20	8.3	100.0
K	107_1L_b2	87.3	5	0.0489	0.0019	0.339	0.175	0.10	73.4	4.2			*	0.09	*	1,200	110	8.1	99.8
K	107_1L_a1	87.1	6.4	0.0494	0.0029	0	0	0.01	73.5	5.4			*	0.093	*	1,500	140	8.0	99.8
K	107_1M_f1	84.7	4.9	0.0499	0.001	0.0236	0.0236	0.00	75.5	4.4			*	0.0034	*	5,000	17	8.0	99.7
K	107_1L_f4	79.2	3.8	0.0478	0.0019	0.179	0.127	0.02	80.9	3.9			*	0.071	*	920	65	8.4	100.0
K	107_1L_f1	78.7	6	0.0526	0.002	0.35	0.194	-0.05	81	6.1			*	0.019	*	1,200	24	7.7	99.4

Table 4. Phanerozoic analytical data from migmatite zircons. Spot analyses are arranged by age from youngest to oldest. Spot-overlap data points have been eliminated from this table.
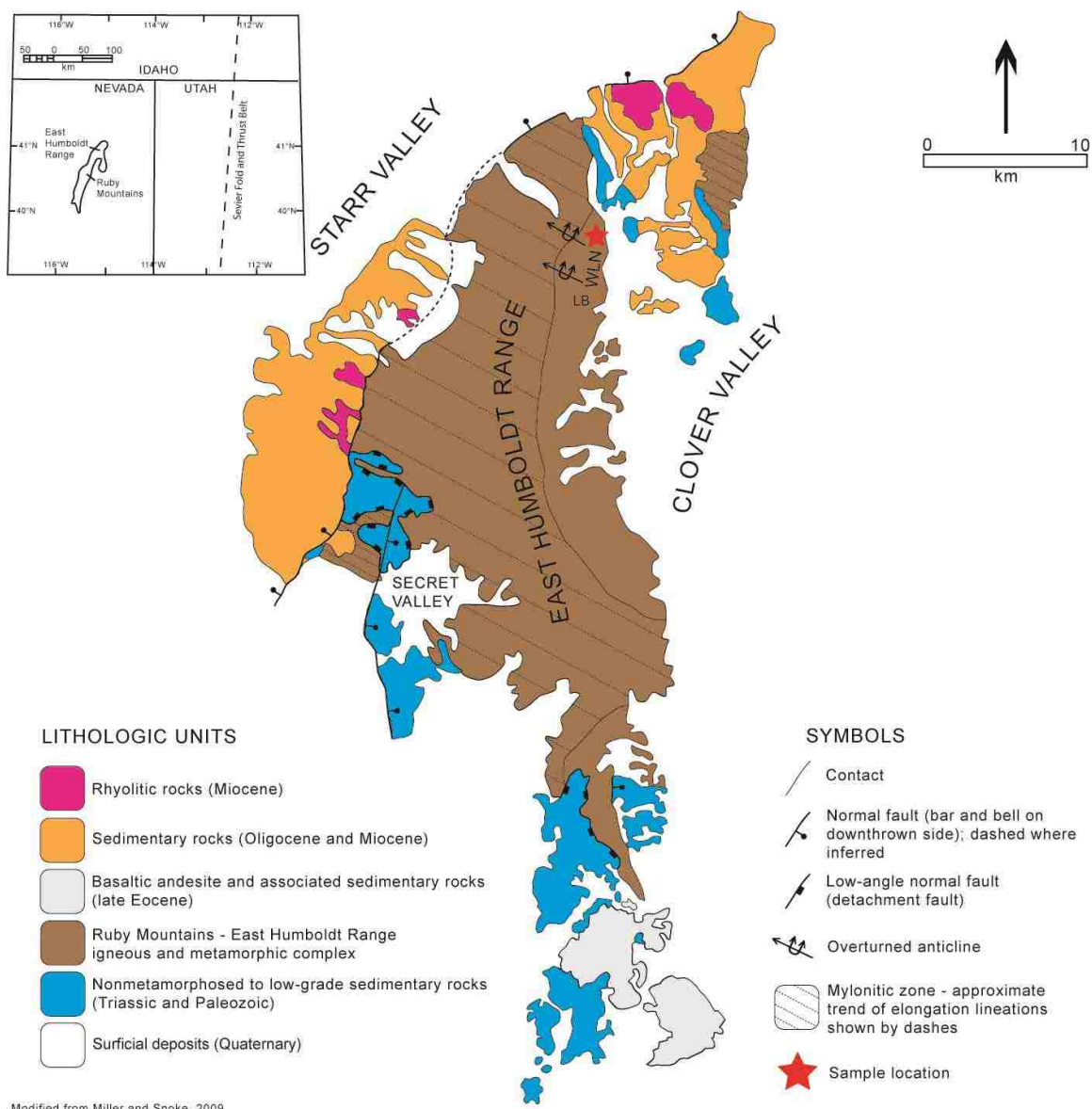
Figure 1. Simplified geologic map of the East Humboldt Range. All Precambrian rocks, including gneisses, schists and calc-silicates, are incorporated into the Ruby Mountains-East Humboldt Range igneous and metamorphic complex. Dashed line on regional map (inset) is the approximate western edge of the Sevier fold-and-thrust belt. Sampling site (red star) was at Angel Lake, on the east flank of the EHR. LB = Lizzies Basin; WLN = Winchell Lake nappe. Modified from Miller and Snoke (2009).
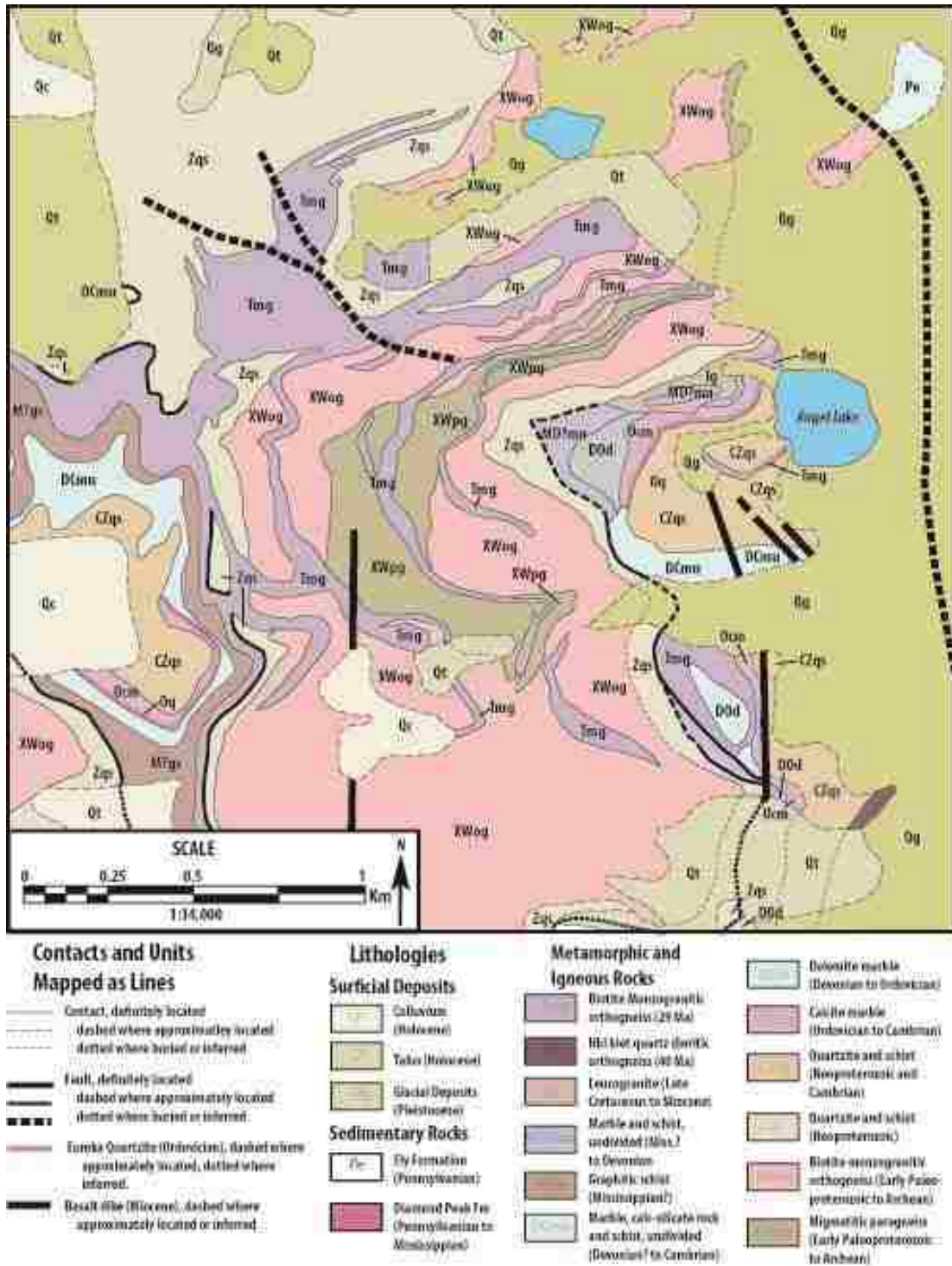
Figure 2. Detailed geologic map of the Angel Lake area. The area corresponds to the red star in Figure 1. Samples were taken from the Neoproterozoic and Cambrian quartzite and schist lithologies (CZqs) west of Angel Lake. Map modified from Henry et al. (2011).
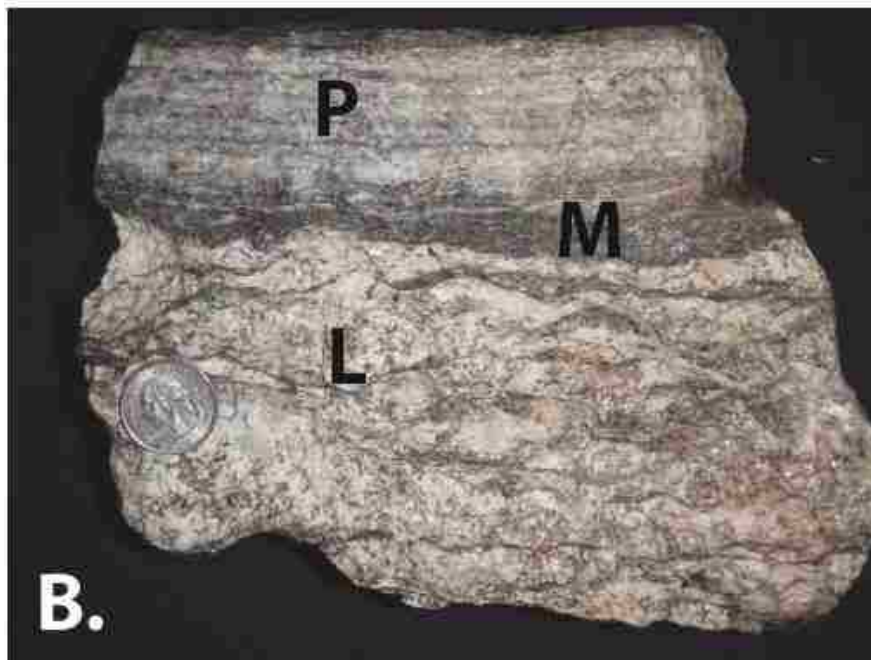
Figure 3. Field photos of samples. (A) Field photo of sample 107-1 showing a leucosome boudin and its accompanying melanosome. (B) Hand sample of 107-4 showing triplet of leucosome, melanosome and paleosome. L = leucosome; M = melanosome; P = paleosome.
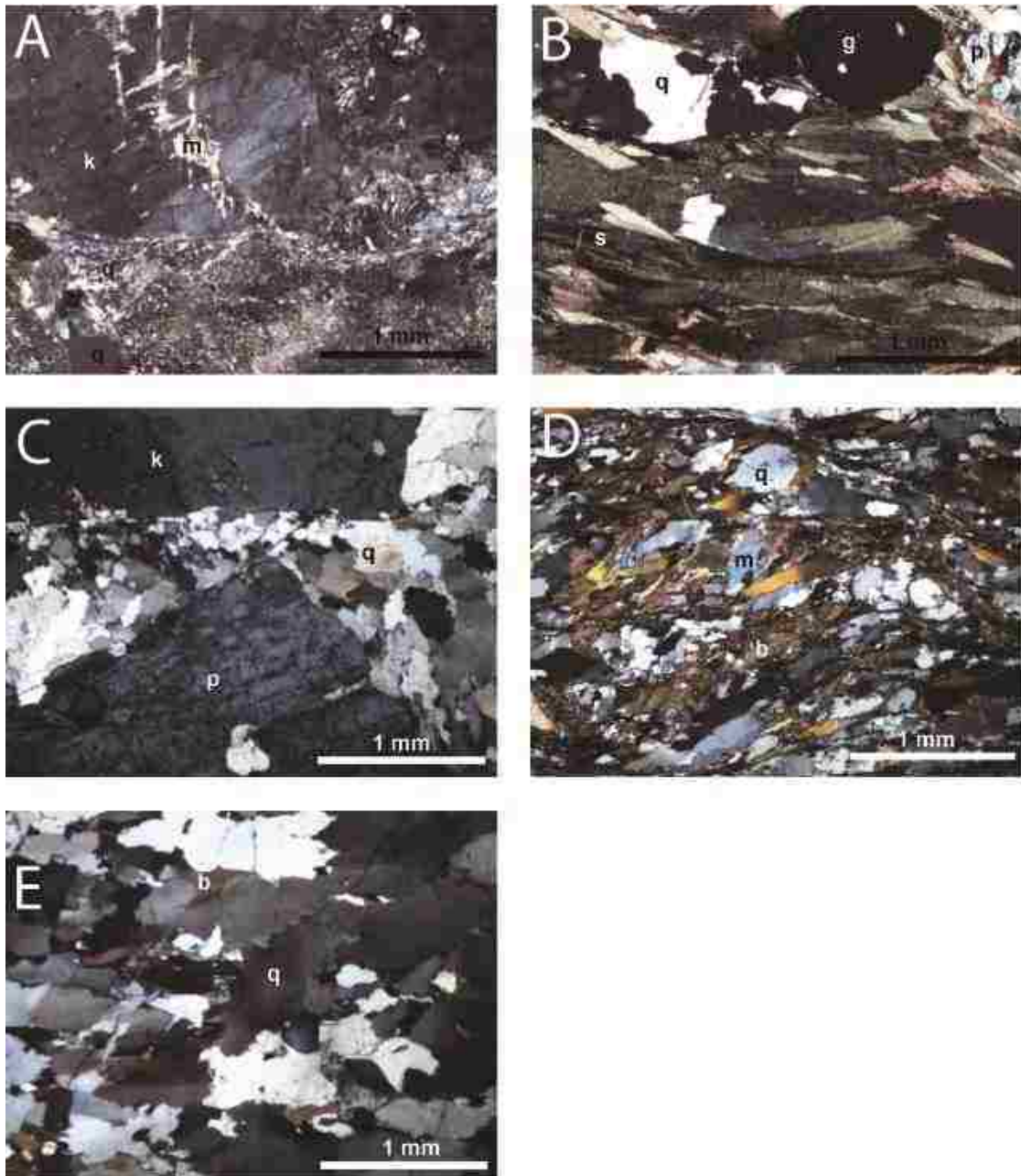
Figure 4. Photomicrographs of thin sections showing representative mineralogy. (A) Photomicrograph of 107-1L. Bottom half of photo shows strained quartz, while upper half of photo shows muscovite growing inside fractured feldspar. (B) Photomicrograph of 107-1M. Bottom half of photo shows biotite with sillimanite. Upper half of photo shows the end of a quartz ribbon, garnet and a twinned plagioclase grain. (C) Photomicrograph of 107-4L. Photo shows subhedral plagioclase and orthoclase grains along with strained quartz. (D) Photomicrograph of 107-4M. This photo shows the more mica-rich domain, although there is a significant percentage of strained quartz in this field of view. (E) Photomicrograph of 107-4Q. Representative view of strained quartz with minor amounts of biotite. k = orthoclase; m = muscovite; q = quartz; g = garnet; s = sillimanite; p = plagioclase; b = biotite.
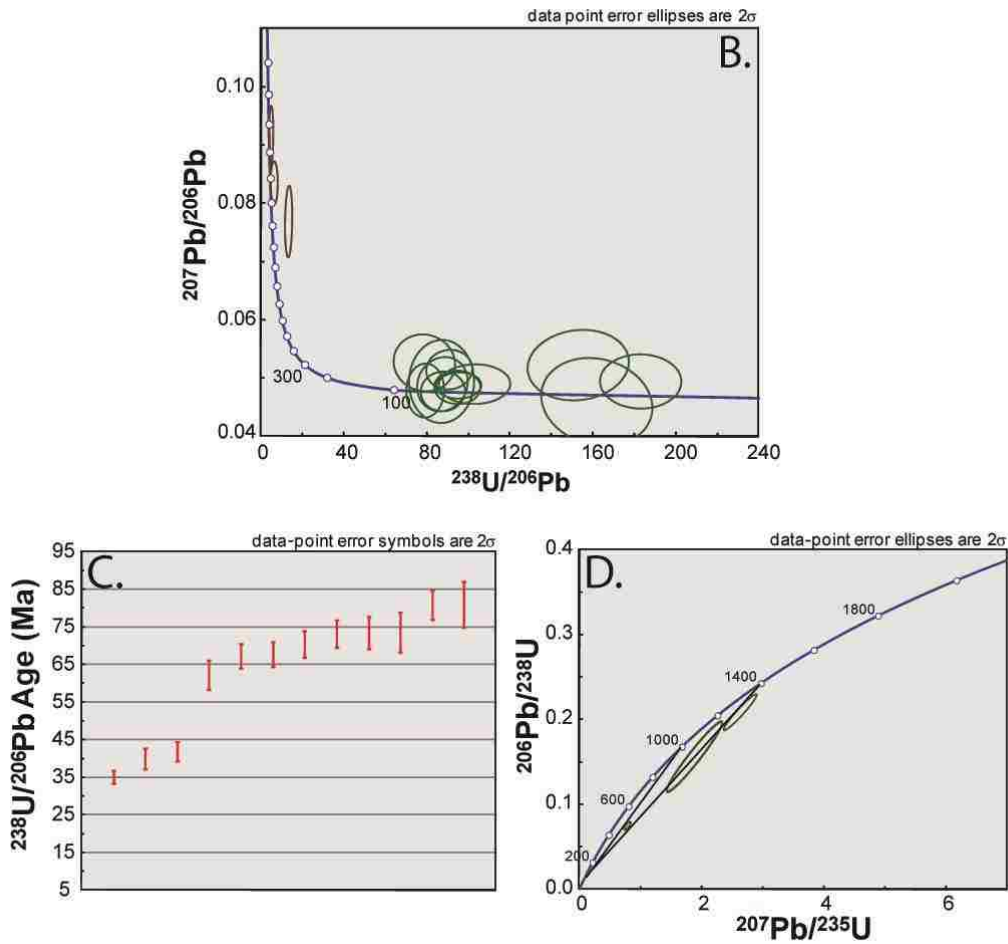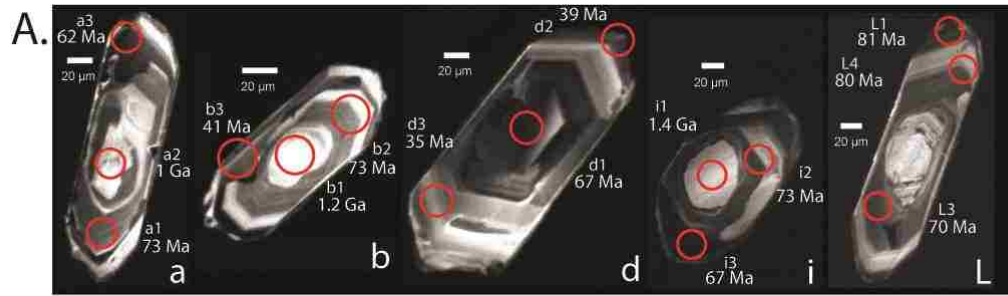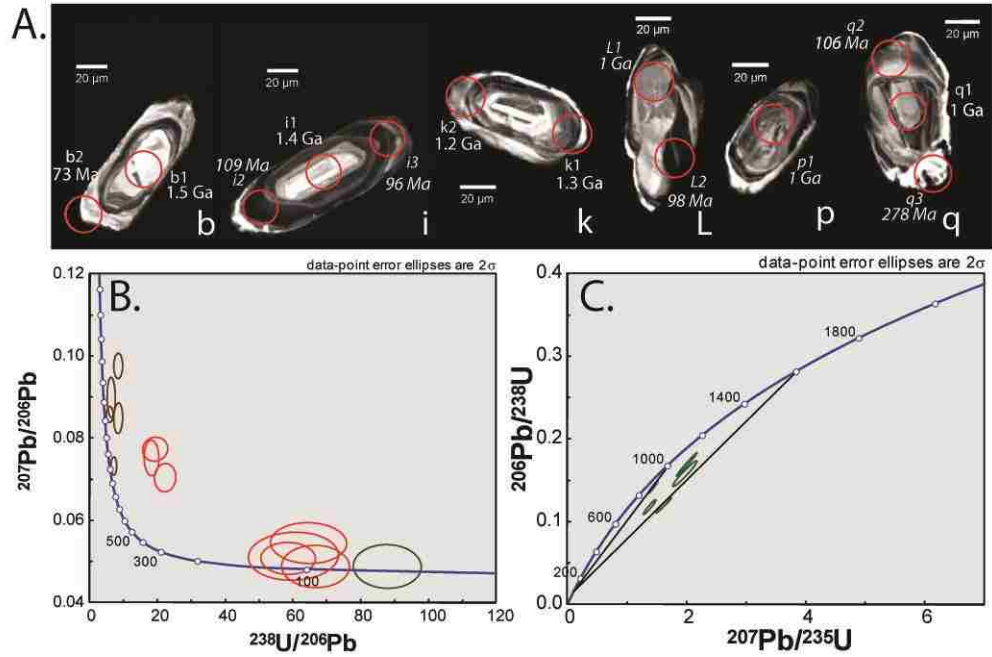
Figure 5. Sample 107-1L geochronology. (A) CL images of dated zircons separated from sample 107-1L. Red circles represent approximate beam placement for spot analysis. (B) Terra-Wasserburg plot with all spot analysis data for sample 107-1L. Brown analyses represent zircon cores and green analyses represent Phanerozoic zircon overgrowths. (C) Age plot for Phanerozoic zircon overgrowths. (D) U-Pb concordia plot with inherited zircon cores from sample 107-1L. Chords have lower intercept pinned at 70 Ma.
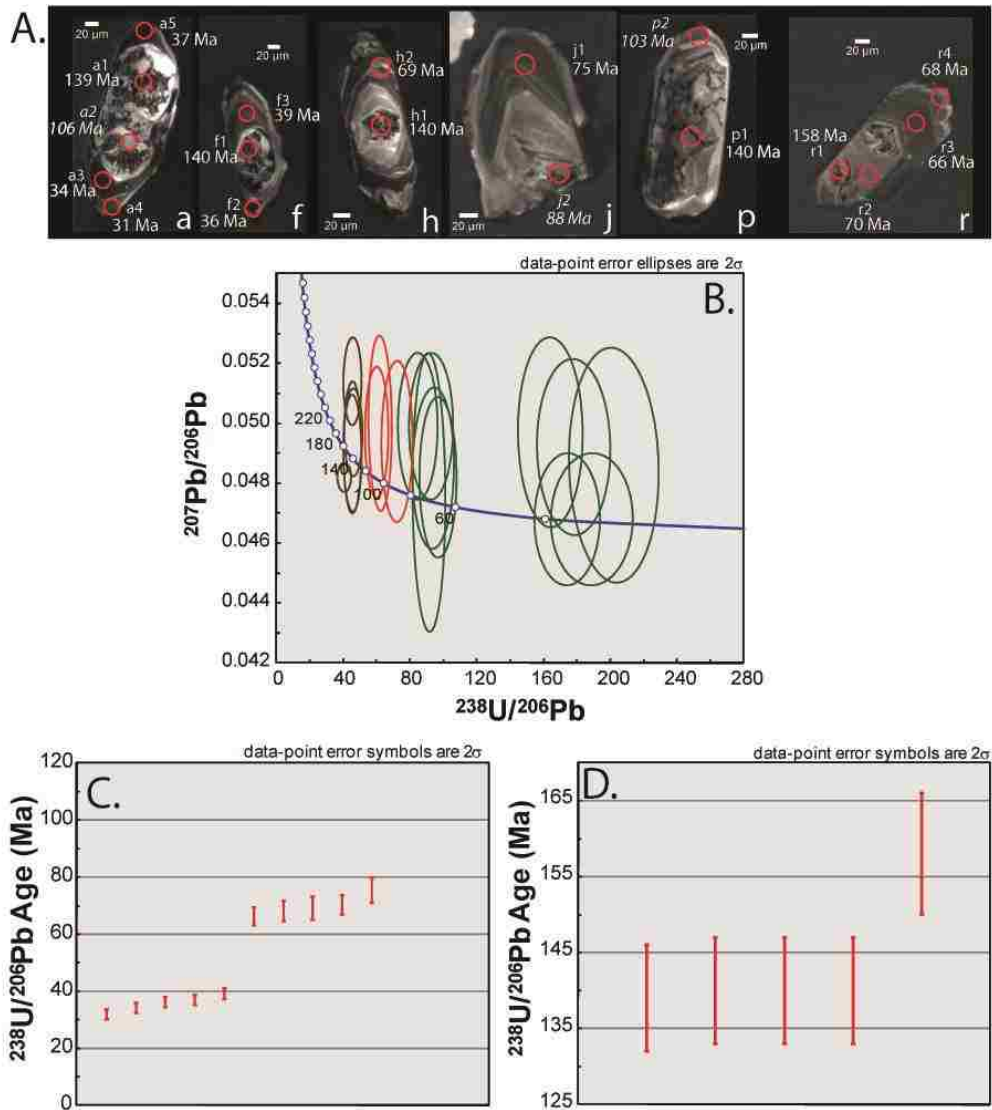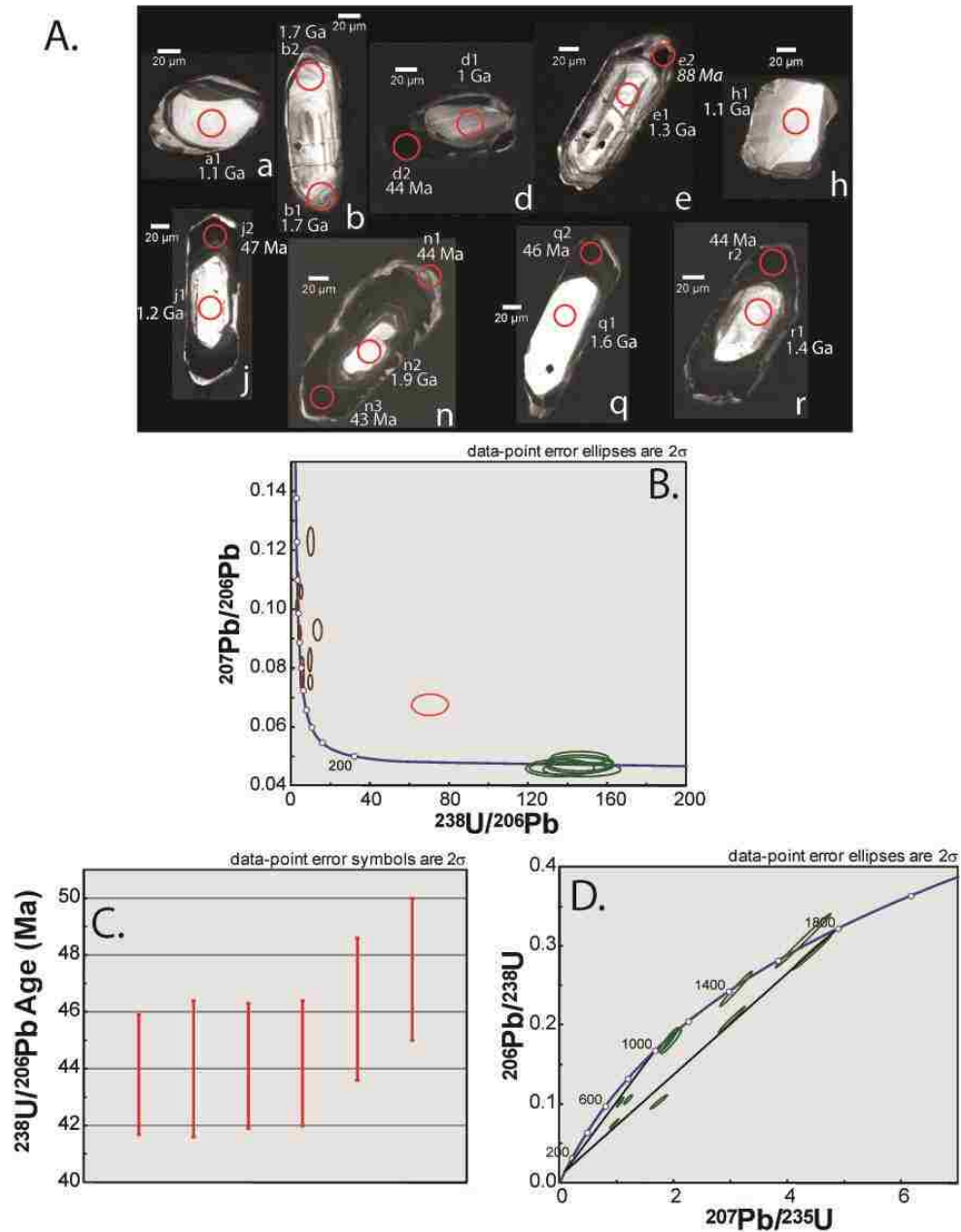
Figure 6. Sample 107-1M geochronology. (A) CL images of dated zircons separated from sample 107-1M. Red circles represent approximate beam placement for spot analysis. Italicized spot analyses and U-Pb dates represent spot-overlap data, which were excluded from the data set so as not to skew geochronology results. (B) Terra-Wasserburg plot with all spot analysis data for sample 107-1M. Brown analyses represent zircon cores, green analyses represent Phanerozoic zircon overgrowths and red analyses represent spot-overlap data, which were excluded from the data set so as not to skew geochronology results. (C) Age plot for Phanerozoic zircon overgrowth. (D) Age plot for the Late Jurassic/Early Cretaceous zircon cores from sample 107-1M.
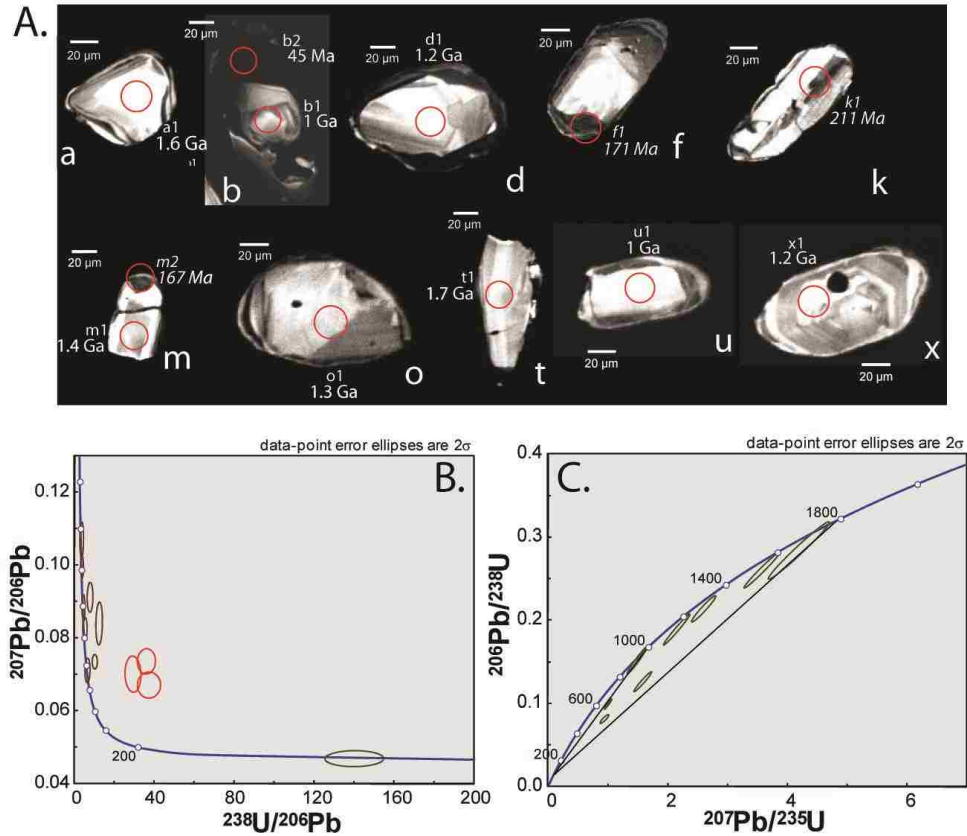
Figure 7. Sample 107-4L geochronology. (A) CL images of dated zircons separated from sample 107-4L. Red circles represent approximate beam placement for spot analysis. Italicized spot analyses and U-Pb dates represent spot-overlap data, which were excluded from the data set so as not to skew geochronology results. (B) Terra-Wasserburg plot with all spot analysis data for sample 107-4L. Brown analyses represent zircon cores, green analyses represent Phanerozoic zircon overgrowths and red analyses represent spot-overlap data, which were excluded from the data set so as not to skew geochronology results. (C) U-Pb concordia plot with inherited zircon cores from sample 107-4L. Chords have lower intercept pinned at 70 Ma

Figure 8. Sample 107-4M geochronology. (A) CL images of dated zircons separated from sample 107-4M. Red circles represent approximate beam placement for spot analysis. Italicized spot analyses and U-Pb dates represent spot-overlap data, which were excluded from the data set so as not to skew geochronology results. (B) Terra-Wasserburg plot with all spot analysis data for sample 107-4M. Brown analyses represent zircon cores, green analyses represent Phanerozoic zircon overgrowths and red analyses represent spot-overlap data, which were excluded from the data set so as not to skew geochronology results. (C) Age plot for Phanerozoic zircon overgrowth. (D) U-Pb concordia plot with inherited zircon cores from sample 107-4M. Chords have lower intercept pinned at 70 Ma.

Figure 9. Sample 107-4Q geochronology. (A) CL images of dated zircons separated from sample 107-4Q. Red circles represent approximate beam placement for spot analysis. Italicized spot analyses and U-Pb dates represent spot-overlap data, which were excluded from the data set so as not to skew geochronology results. (B) Terra-Wasserburg plot with all spot analysis data for sample 107-4Q. Brown analyses represent zircon cores, green analyses represent Phanerozoic zircon overgrowths and red analyses represent spot-overlap data, which were excluded from the data set so as not to skew geochronology results. (C) U-Pb concordia plot with inherited zircon cores from sample 107-4M. Chords have lower intercept pinned at 70 Ma.
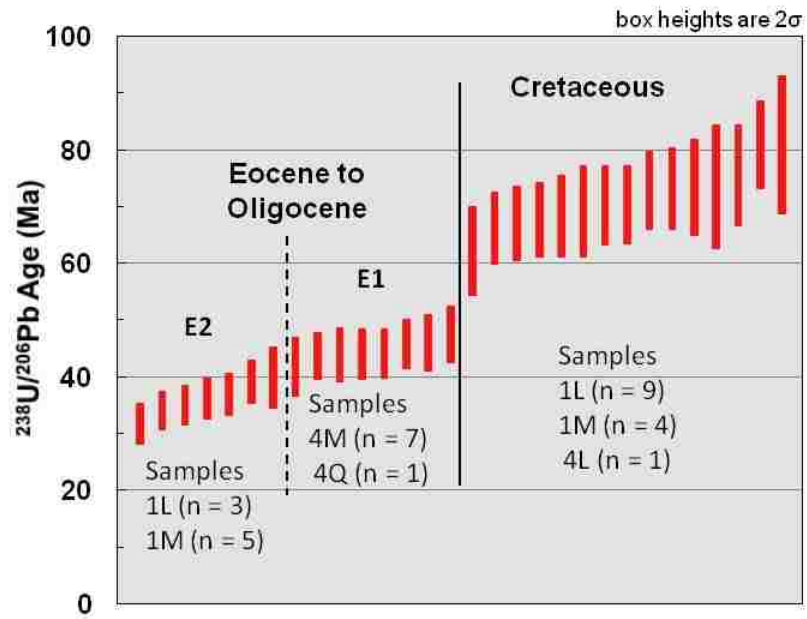
Figure 10. Phanerozoic overgrowth ages. Plots all Phanerozoic overgrowths (except data determined to be spot-overlap and Phanerozoic cores from sample 107-1M). Black lines delineate the three age populations (K, E1 and E2). E2 appears to be an age gradient, while K and E1 appear to be single-age populations.
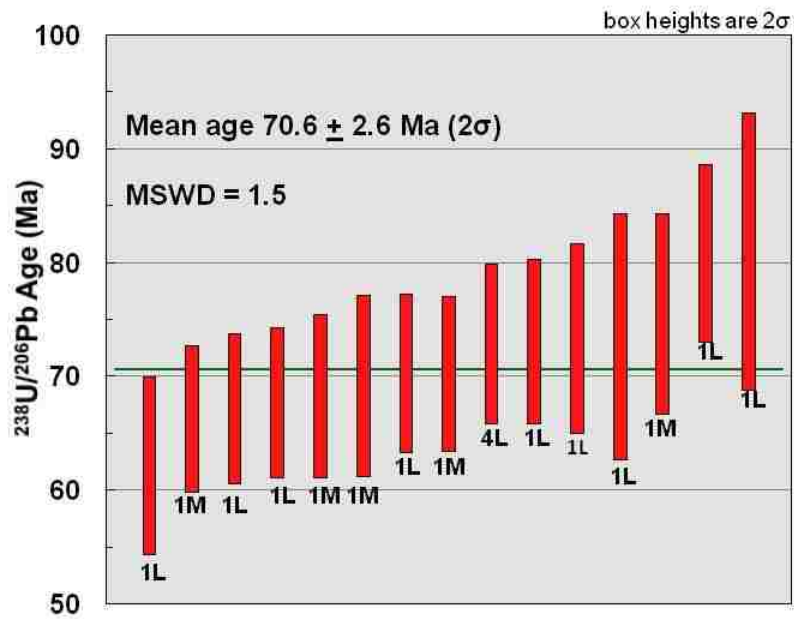
Figure 11. K age plot. Weighted mean ^{238}U/^{206}Pb age plot of the 15 Cretaceous zircon overgrowth ages; maximum acceptable MSWD for a population of n = 15 is 1.784 (Wendt and Carl, 1991). Population contains nine ages from leucosome sample 1L, five ages from melanosome sample 1M and one age from melanosome sample 4M.
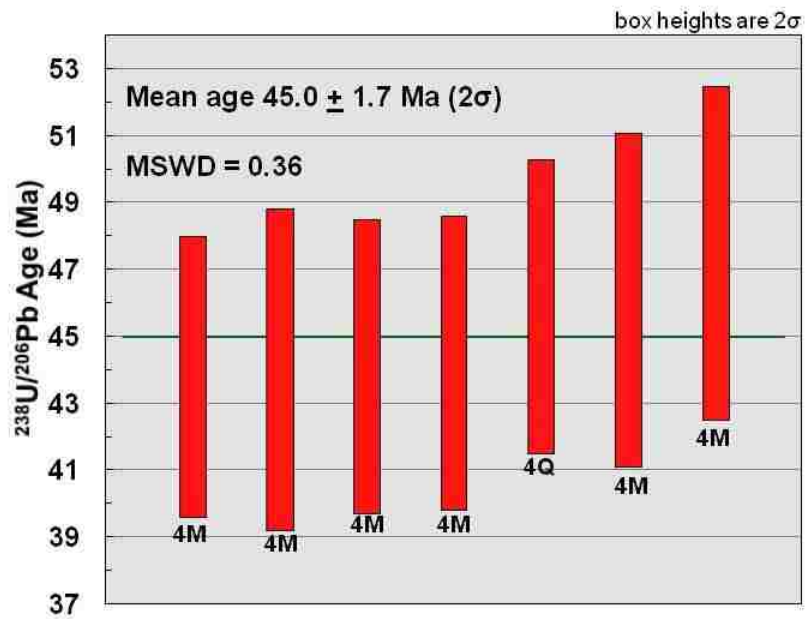
Figure 12. E1 age plot. Plots a statistically significant single-age population at 45 ± 1.3 Ma; maximum acceptable MSWD for a population of n = 7 is 2.265 (Wendt and Carl, 1991). Population includes six ages from melanosome sample 4M and one age from paleosome sample 4Q.
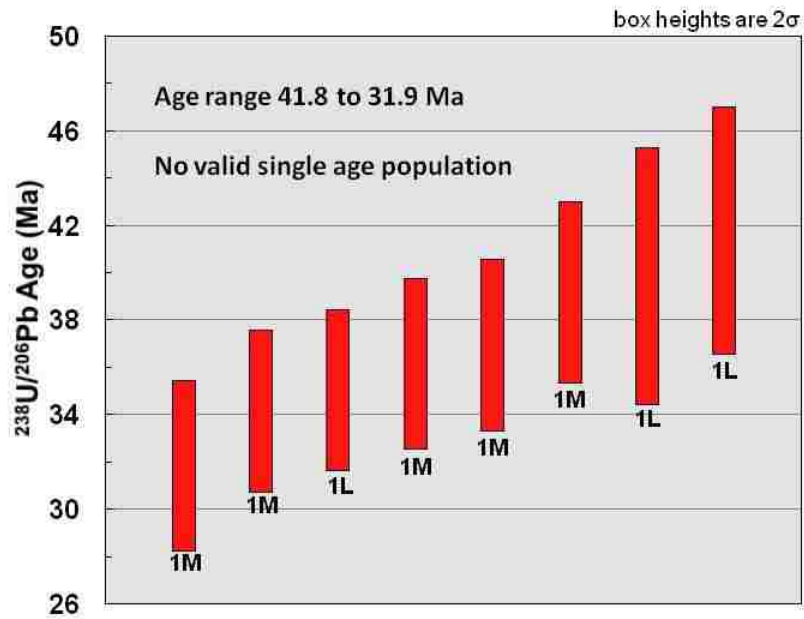
Figure 13. E2 age range plot. Plots a range of ages from 41.8 ± 2.6 Ma to 31.9 ± 1.8 Ma. A mean weighted age of 36.2 ± 2.5 Ma was calculated for this population with a MSWD of 2.4; the maximum acceptable MSWD for a population of n = 8 is 2.155 (Wendt and Carl, 1991) so this age in not statistically significant. This population includes five ages from melanosome sample 1M and three ages from leucosome sample 1L.
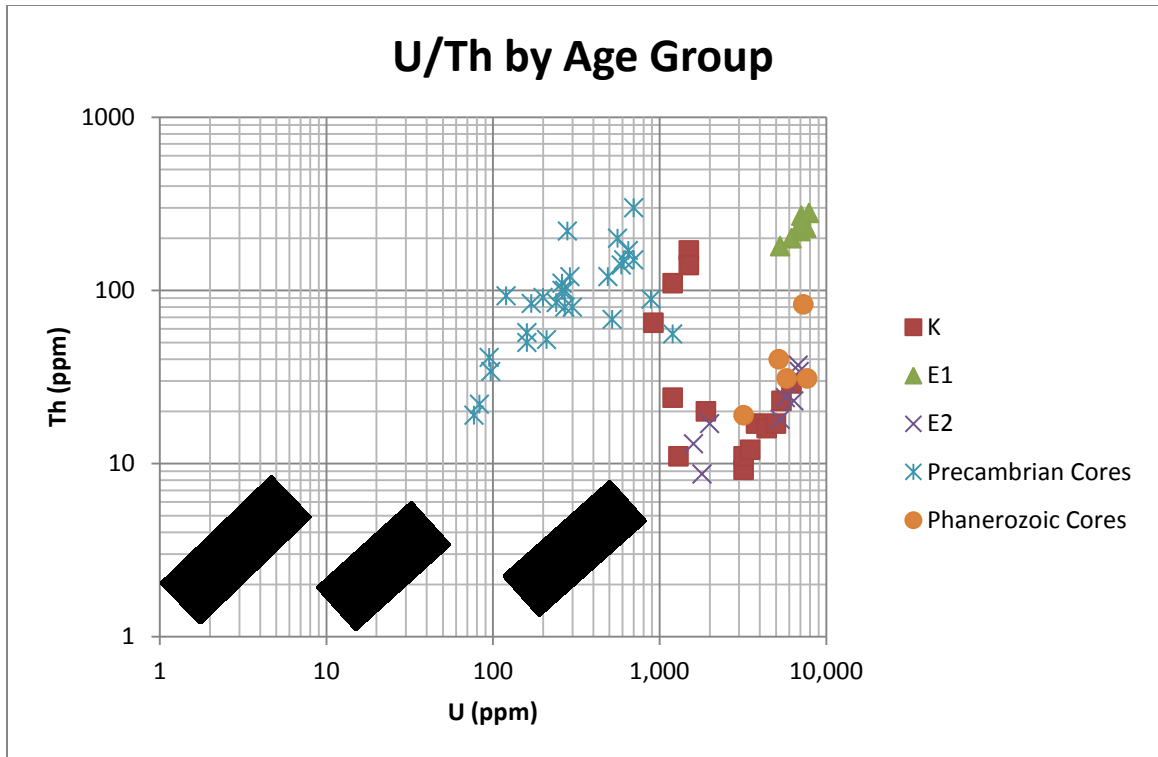
Figure 14. Th/U plot by age grouping. Plots Phanerozoic overgrowths (except data determined to be spot-overlap), Precambrian cores and Phanerozoic cores.
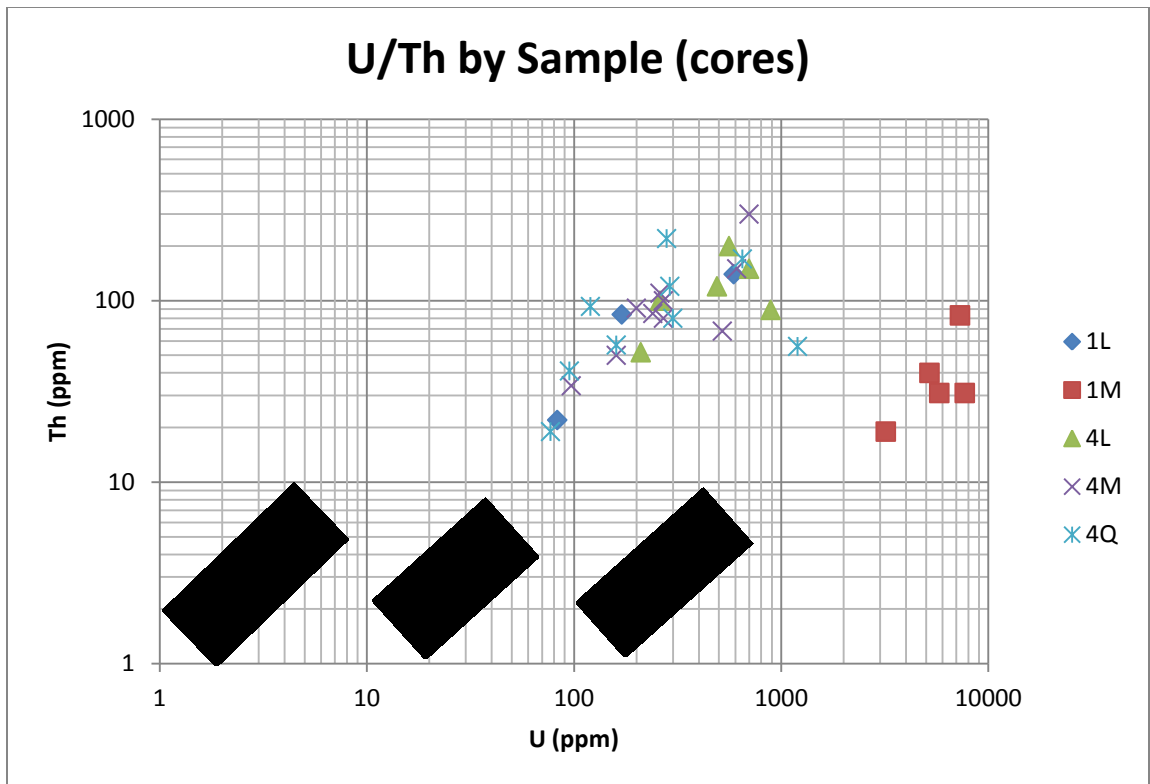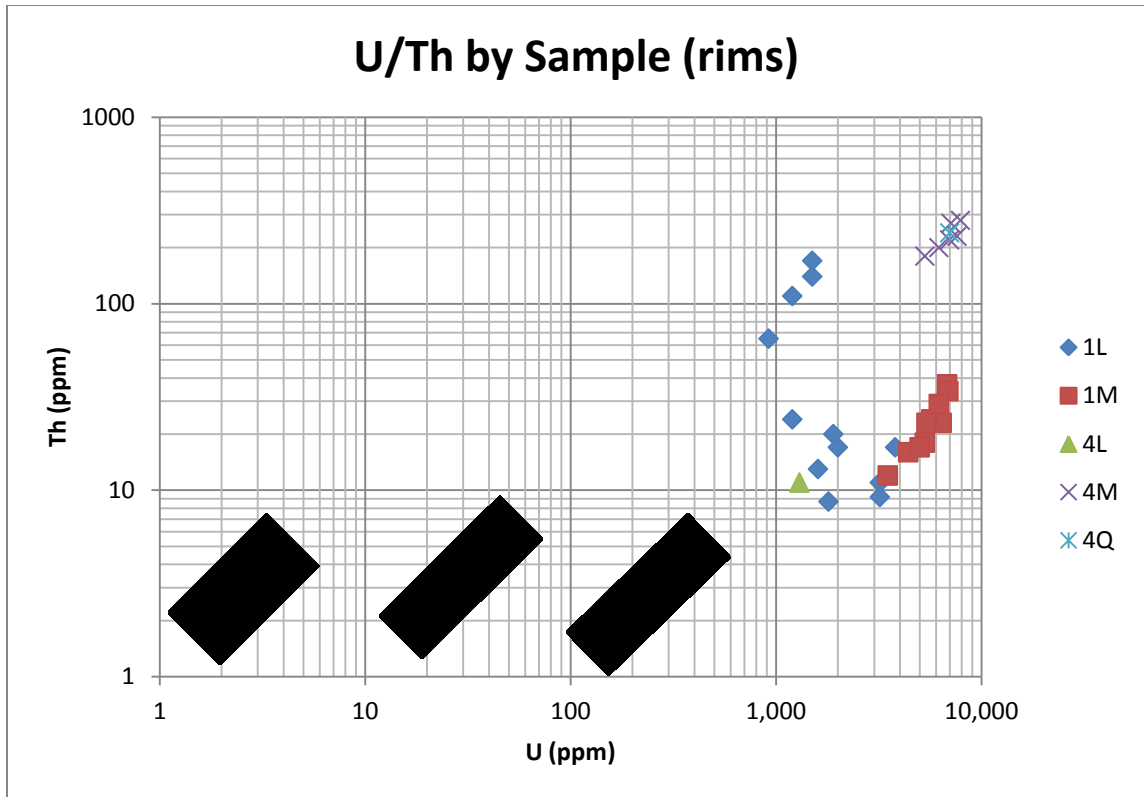
Figure 15. Th/U plot of zircon cores.

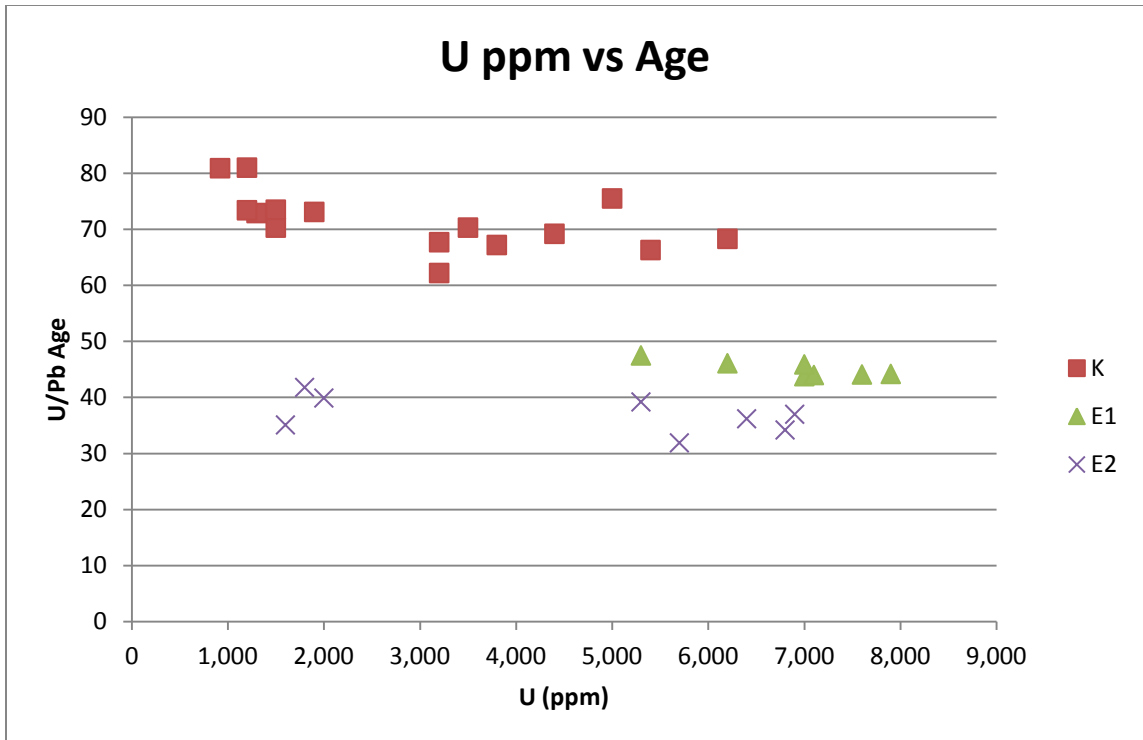Figure 16. Th/U plot of Phanerozoic zircon overgrowths.

Figure 17. U(ppm) vs. U/Pb age plot. Plots $^{206}Pb/^{238}U$ age vs. U content. Each age group appears to have a wide spread of U content.
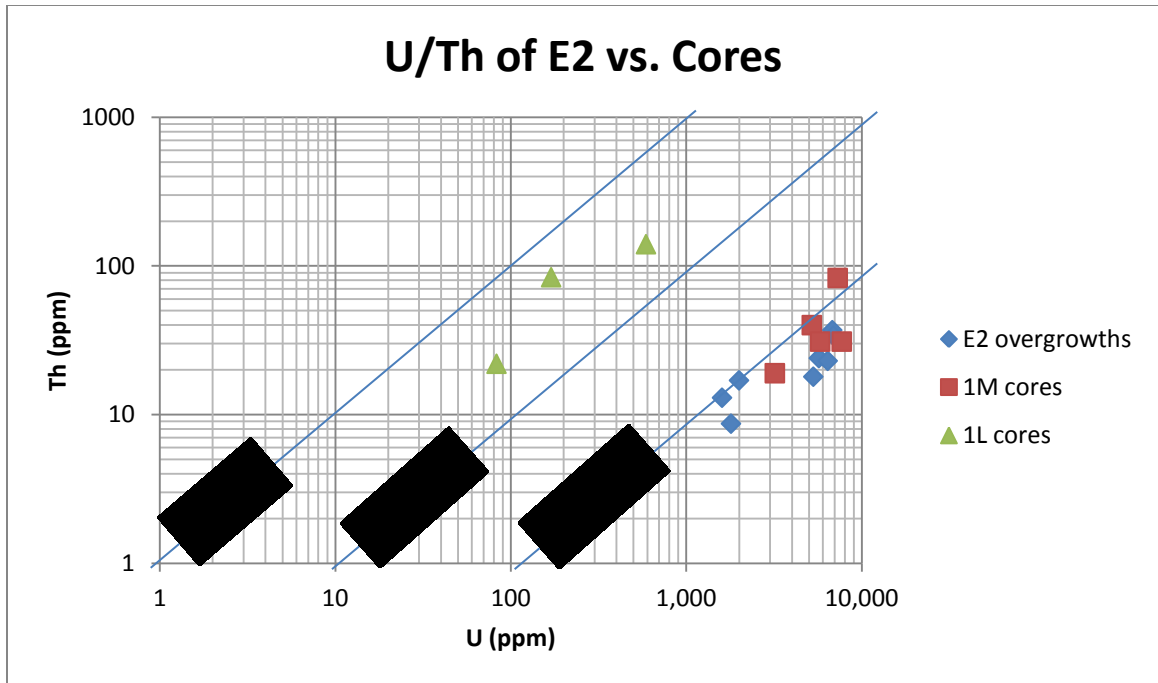
Figure 18. Th/U of overgrowths vs. cores. Plots the E2 zircon overgrowths vs. the 1M and 1L cores they surround.
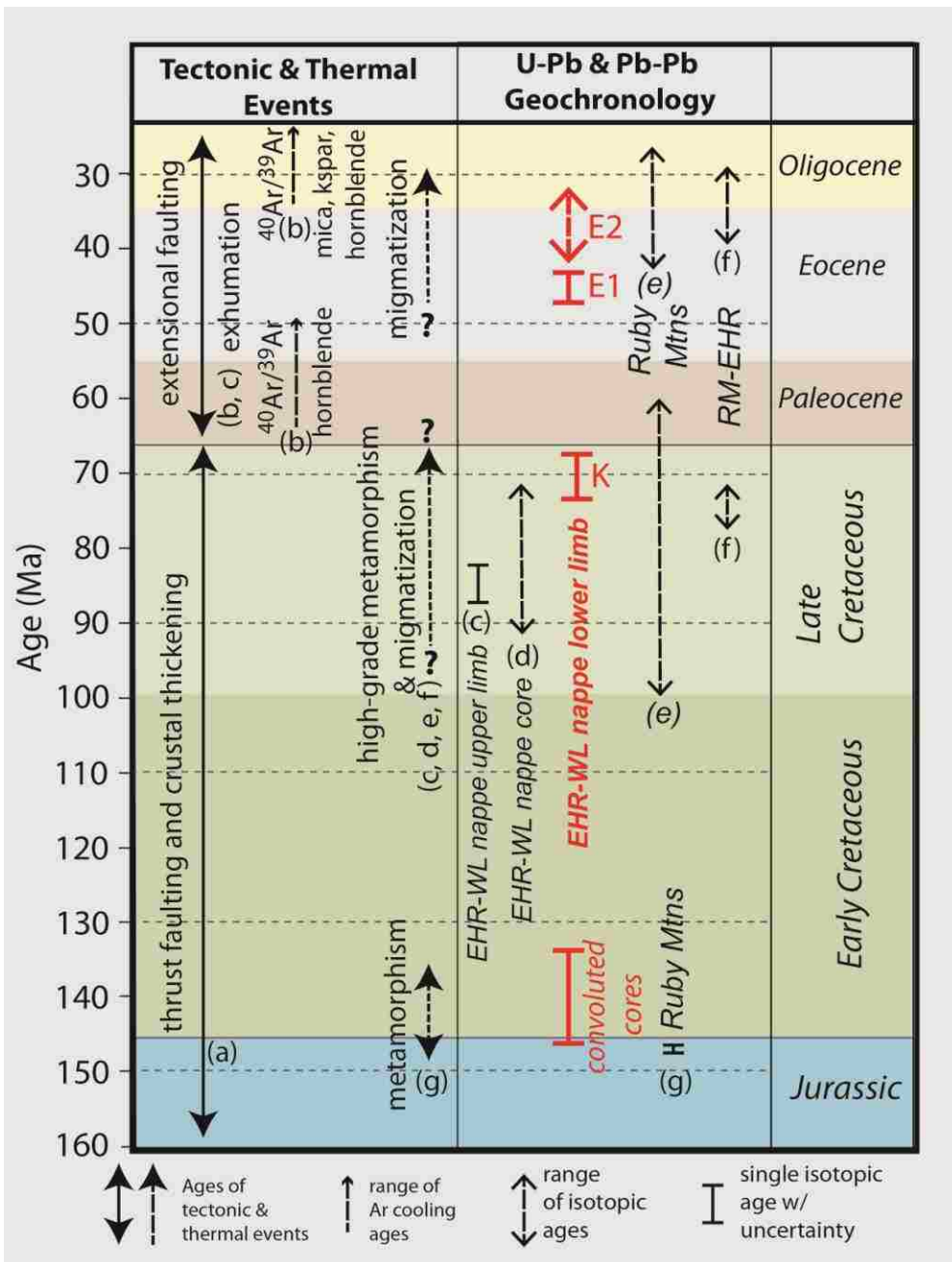
Figure 19. Comparison of isotopic ages and the timing of tectonic events. Summary of published isotopic ages, new ages from this study and inferred tectonic events ruby Mountain-East Humboldt Range metamorphic core complex. Ages shown in red are results from this study. Data sources include (a) DeCelles (2004), (b) McGrew & Snee (1994), (c) McGrew et al. (2000), (d) Premo et al. (2008), (e) Howard et al. (2011), (f) Wright & Snoke (1993), and (g) Hudec and Wright (1991). New ages from this study are shown in read, K = Cretaceous ages, E1 = Eocene age average, E2 = range of Eocene ages, see text for discussion. RM-EHR = Ruby Mountains-East Humboldt Range; EHR-WL nappe = Winchell Lake nappe in East Humboldt Range.

REFERENCES

Bea, F. and Montero, P., 1999, Behavior of accessory phases and redistribution of Zr, REE, Y, Th
and U during metamorphism and partial melting of metapelites in the lower crust: An
example from the Kinzigite Formation of Ivrea-Verbano, NW Italy. *Geochimica et
Cosmochimica Act*, v. 63, p. 1133-1153.

Camilleri, P.A., and Chamberlain, K.R., 1997, Mesozoic tectonics and metamorphism in the
Pequop Mountains and Wood Hills region, northeast Nevada: Implications for the
architecture and evolution of the Sevier orogen. *Geological Society of America Bulletin*,
v.109, p. 74-94.

Corfu, F., Hanchar, J.M., Hoskin, P.W.O., and Kinny, P., 2003, Atlas of Zircon Textures. *Reviews in
Mineralogy and Geochemistry: Zircon*, v. 53, p. 469-500.

Dallmeyer, R.D., Snoke, A.W., and McKee, E.H., 1986, The Mesozoic-Cenozoic tectonothermal
evolution of the Ruby Mountains, East Humboldt Range, Nevada: A Cordilleran
metamorphic core complex. *Tectonics*, v. 5, p. 931-954.

Dokka, R.K., Mahaffie, M.J., and Snoke, A.W., 1986, Thermochronologic evidence of major
tectonic denudation associated with detachment faulting, northern Ruby Mountains-East
Humboldt Range, Nevada. *Tectonics*, v.5, p. 995-1006.

DeCelles, P.G, 2004, Late Jurassic to Eocene evolution of the Cordilleran thrust belt and foreland
basin system, western U.S.A. *American Journal of Science*, v. 304, p. 105-168.

Harley, S.L., Kelly, N.M., and Möller, A., 2007, Zircon Behavior and the Thermal Histories of
Mountain Chains. *Elements*, v. 3, p. 25-30.

Harrison, T.M., and Watson, E.B., 1983, Kinetics of zircon dissolution and zirconium diffusion in
granitic melts of variable water content. *Contributions to Mineralogy and Petrology*, v. 84, p.
66-72.

Henry, C.D., McGrew, A.J., Colgan, J.P., Snoke, A.W., and Brueseke, M.E., 2011, Timing, distribution, amount, and style of Cenozoic extension in the northern Great Basin, *in* Lee, J., and Evans, J.P., eds., Geologic Field Trips to the Basin and Range, Rocky Mountains, Snake River Plain, and Terranes of the U.S. Cordillera: Geological Society of America Field Guide 21, p. 27-66.

Hermann, J., and Rubatto, D., 2003, Relating zircon and monazite domains to garnet growth zones: age and duration of granulite facies metamorphism in the Val Malenco lower crust. *Journal of Metamorphic Petrology*, v. 21, p. 833-852.

Hodges, K.V., Snoke, A.W., and Hurlow, H.A., 1992, Thermal evolution of a portion of the Sevier hinterland: The northern Ruby Mountains-East Humboldt Range and Wood Hills, northeastern Nevada. *Tectonics*, v. 11, no. 1, p. 154-164.

Hoskin, P.W.O, and Schaltegger, U., 2003, The composition of zircon and igneous and metamorphic petrogenesis, in: *Reviews in Mineralogy and Geochemistry: Zircon*, v. 53, p. 2-62.

Howard, K.A., Wooden, J.L., Barnes, C.G., Premo, W.R., Snoke, A.W., and Lee, S.Y., 2011, Episodic growth of a Late Cretaceous and Paleogene intrusive complex of pegmatitic leucogranite, Ruby Mountains core complex, Nevada, USA. *Geosphere*, v. 7, no. 5, p. 1220-1248.

Hudec, M.R., 1990, The structural and thermal evolution of the central Ruby Mountains, Elko County, Nevada [Ph.D. dissertation]: Laramie, University of Wyoming, 272 p.

Hurlow, H.A., Snoke, A.W., and Hodges, K.V., 1991, Temperature and pressure of mylonitization in a Tertiary extensional shear zone, Ruby Mountains-East Humboldt Range, Nevada: Tectonic implications. *Geology*, v. 19, p. 82-86

Kistler, R.W., Ghent, E.D., and O'Neill, J.R., 1981, Petrogenesis of garnet two-mica granites in the Ruby Mountains, Nevada. *Journal of Geophysical Research*, v. 86, p. 10591-10606.

Kruckenberg, S.C., Whitney, D.L., Teyssier, C., Fanning, C.M., and Dunlap, W.J., 2008, Paleocene-Eocene migmatite crystallization, extension, and exhumation in the hinterland of the northern Cordillera: Okanogan dome, Washington, USA. *GSA Bulletin*, v. 120, no. 7/8, p. 912-929.

Lee, S. Y., Barnes, C. G., Snoke, A. W., Howard, K. A., and Frost, C. D., 2003, Petrogenesis of Mesozoic, peraluminous granites in the Lamoille Canyon area, Ruby Mountains, Nevada, USA. *Journal of Petrology*, v. 44, no. 4, p. 713–732.

Lush, A.P., McGrew, A.J., Snoke, A.W., and Wright, J.E., 1988, Allochthonous Archean basement in the East Humboldt Range, Nevada. *Geology*, v. 16, p. 349-353.

McGrew, A.J., 1992, Tectonic evolution of the northern East Humboldt Range, Elko County, Nevada [Ph.D. dissertation]: Laramie, University of Wyoming, 191 p.

McGrew, A.J., Peters, M.T., and Wright, J.E., 2000, Thermobarometric constraints on the tectonothermal evolution of the East Humboldt Range metamorphic core complex, Nevada. *GSA Bulletin*, v. 112, no. 1, p. 45-60.

McGrew, A.J., and Snoke, A.W., 2010, SHRIMP-RG U-Pb isotopic systematic of zircon from the Angel Lake orthogneiss, East Humboldt Range, Nevada: Is this really Archean crust?: COMMENT. *Geosphere*, v.6., no. 6, p. 962-965.

McGrew, A.J., and Premo, W.R., 2011, The Angel Lake gneiss complex of northeastern Nevada and the southwestern limits of Archean to Paleoproterozoic basement in North America. *Geological Society of America Abstracts with Programs*, v. 43, no. 5, p. 435.

Miller, C.F., and Bradfish, L.J, 1980, An inner Cordillera belt of muscovite-bearing plutons> Geology, v. 8, p.412-416.

Miller, C.F., McDowell, S.M., and Mapes, R.W., 2003, Hot and Cold Granites? Implications of
zircon saturation temperatures and preservation of inheritance. *Geology*, v. 31, no. 6, p.
529-532.

Miller, R.B., and Snoke, A.W., 2009, The utility of crustal cross sections in the analysis of
orogenic processes in contrasting tectonic settings. *Crustal Cross Sections from the Western
North American Cordillera and Elsewhere: Implications for Tectonic and Petrologic Processes*.
Geological Society of America Special Paper 456, p. 1-38.

Nasdala, L., Zhang, M., Kempe, U., Panczer, G., Gaft, M., Andrut, M., and Plötze, M., 2003,
Spectroscopic methods applied to zircon, in: *Reviews in Mineralogy and Geochemistry:
Zircon*, v. 53, p. 427-467.

Nemchin, A.A., Giannini, L.M., Bodorkos, S., and Oliver, N.H.S., 2001, Ostwald ripening as a
possible mechanism for zircon overgrowth formation during anatexis: Theoretical
constraints, a numerical model, and its application to pelitic migmatites of the Tickalara
Metamorphics, Northwestern Australia. *Geochimica et Cosmochimica Acta*, v. 65, p. 2771-
2787.

Peters, M. T., and Wickham, S. M., 1994, Petrology of upper amphibolite facies marbles from the
East Humboldt Range, Nevada, USA: Evidence for high temperature, retrograde, hydrous
volatile fluxes at mid-crustal levels. *Journal of Petrology*, v. 35, p. 205–238.

Premo, W.R., Castineiras, P., and Wooden, J.L., 2008, SHRIMP-RG U-Pb isotopic systematic of
zircon from the Angel Lake orthogneiss, East Humboldt Range, Nevada: Is this really Archean
crust? *Geosphere*, v. 4, no. 6, p. 963-975.

Premo, W.R., Castineiras, P., and Wooden, J.L., 2010, SHRIMP-RG U-Pb isotopic systematic of
zircon from the Angel Lake orthogneiss, East Humboldt Range, Nevada: Is this really Archean
crust?: REPLY. *Geosphere*, v. 6, no. 6, p. 966-972.

Sawyer, E.W., 1996, Melt segregation and magma flow in migmatites: Implications for the generation of granite magmas. *Transactions of the Royal Society of Edinburgh, Earth Sciences*, v.87, p. 85-94.

Sawyer, E.W., 2008, Atlas of Migmatites. *The Canadian Mineralogist, Special Publication #9, Quebec.* 386 p.

Schmitt, A.K, Grove, M., Harrison, T.M., Lovera, O.M., Hulen, J. and Waters, M., 2003, The Geysers - Cobb Mountain Magma System, California (Part 1): U-Pb zircon ages of volcanic rocks, conditions of zircon crystallization and magma residence times. *Geochimica et Cosmochimica Acta*, v. 67, no. 18, p. 3423-3442.

Thorman, C.H., and Snee, L.W., 1988, Thermochronology of metamorphic rocks in the Wood Hills and Pequop Mountain, northeastern Nevada. *Geological Society of America Abstracts with Programs*, v. 20, p. A18.

Vavra, G., Gebauer, D., Schmid, R., and Compston, W., 1996, Multiple zircon growth and recrystallization during polyphase Late Carboniferous to Triassic metamorphism in granulites of the Ivrea Zone (Southern Alps): An ion microprobe (SHRIMP) study. *Contributions to Mineralogy and Petrology*, v. 122, p. 337-358.

Vavra, G., Schmid, R., and Gebauer, D., 1998, Internal morphology, habit and U-Th-Pb microanalysis of amphibolite-to-granulite facies zircons: geochronology of the Ivrea Zone (Southern Alps). *Contributions to Mineralogy and Petrology*, v. 134, p. 380-404.

Vernon, R.H., and Clarke, G.L., 2008, Principles of Metamorphic Petrology. 446 p.

Watson, E.B, and Harrison, T.M., 1983, Zircon saturation revisited: temperature and composition effects in a variety of crustal magma types. *Earth and Planetary Science Letters*, v. 64, p. 295-304.

Watson, E.B., Vicenzi, E.P., and Rapp, R.P., 1989, Inclusion/host relations involving accessory

   minerals in high-grade metamorphic and anatectic rocks. *Contributions to Mineralogy and*

   Petrology, v. 101, p. 220-231.

Watson, E.B., 1996, Dissolution, growth and survival of zircons during crustal fusion: Kinetic

   principles, geological models and implications for isotopic inheritance. *Royal Society of*

   Edinburgh Transaction, Earth Sciences, v. 87, p. 43-56.

Watt, G.R., and Harley, S.L., 1993, Accessory phase controls on the geochemistry of crustal melts

   and restites produced during water-undersaturated partial melting. *Contributions to*

   Mineralogy and Petrology, v. 114, p. 550-566.

Watt, G.R., Burns, I.M., and Graham, G.A., 1996, Chemical characteristics of migmatites:

   Accessory phase distribution and evidence for fast melt segregation rates. *Contributions to*

   Mineralogy and Petrology, v. 125, p. 100-111.

Wells, M.L., and Hoisch, T.D., 2008, The role of mantle delamination in widespread Late

   Cretaceous extension and magmatism in the Cordilleran orogen, western United States.

   Geological Society of America Bulletin, v. 120, p. 515-530.

Wendt, I and Carl, C. 1991, The statistical distribution of mean squared weighted deviation.

   Chemical Geology, v. 86, p. 275-285.

Wright, J.E., and Snoke, A.W., 1993, Tertiary magmatism and mylonitization in the Ruby–East

   Humboldt metamorphic core complex, northeastern Nevada: U-Pb geochronology and Sr,

   Nd, Pb isotope geochemistry. *Geological Society of America Bulletin*, v. 105, p. 935–952.

CURRICULUM VITAE

Graduate College
University of Nevada, Las Vegas

Jordan Drew

Degrees:
 Bachelor of Arts, Earth and Environmental Science 2009
 University of Kentucky

Thesis Title: Cretaceous and Eocene U-Pb Zircon Migmatite Ages from the East Humboldt Range
 Metamorphic Core Complex, Nevada

Thesis Examination Committee:
 Committee Chairperson, Rodney V. Metcalf, Ph.D.
 Committee Member, Michael Wells, Ph.D.
 Committee Member, Terry Spell, Ph.D.
 Graduate Faculty Representative, George Rhee, Ph.D.